International Communications in Heat and Mass Transfer 180 (2026) 112469

Contents lists available at ScienceDirect

International Communications in Heat and Mass Transfer

journal homepage: www.elsevier.com/locate/ichmt

Thermal enhancement of PCM-based latent heat storage with perforated fin networks and coupled effects of geometry, natural convection, and PCM melting using MLP/GA optimization

Motrih Al-Mutiry [a,*], Hyder H. Abed Balla [b], Mohamed Arbi Khlifi [c,*], Banaz Shahab Haji [d], Mohammad Abdulhadi O. Althobaiti [e], Ashrf althbiti [f], Norah Alsairy [g], Hanaa Abu-Zinadah [h,*], Duc Chuan Nguyen [i,*], Ibrahim Mahariq [j,k,l,m,**]

[a] *Department of Geography and Environmental Sustainability, College of Humanities and Social Sciences, Princess Nourah bint Abdulrahman University, 11671 Riyadh, Saudi Arabia*
[b] *Department of Unmanned Aviation Technical Engineering, Najaf polytechnic College, Al Furat Al Awsat Technical University, Najaf, Iraq*
[c] *Department of Electrical Engineering, Faculty of Engineering, Islamic University of Madinah, Madinah 42351, Saudi Arabia*
[d] *Medical Radiology Imaging Department, College of Health Sciences, Lebanese French University (LFU), Kurdistan Region, Erbil, Iraq*
[e] *Department of Foreign Languages, College of Arts, Taif University, Taif 21944, Saudi Arabia*
[f] *Department of Information Technology, College of Computers and Information Technology, Taif University, Taif 21944, Saudi Arabia*
[g] *Department of Physics, College of Turabah, Taif University, P.O. Box 11099, Taif 21944, Saudi Arabia*
[h] *Department of Mathematics and Statistics, College of science, University of Jeddah, Jeddah, Saudi Arabia*
[i] *Institute of Maritime, University of Transport Ho Chi Minh City, Ho Chi Minh City, Viet Nam*
[j] *College of Engineering and Architecture, Gulf University for Science and Technology, Mishref, Kuwait*
[k] *Department of Electrical and Electronic Engineering, Faculty of Engineering and Architecture, Istanbul Gelisim University, Avcılar- Istanbul, 34310, Istanbul, Türkiye*
[l] *Department of Medical Research, China Medical University Hospital, China Medical University, Taichung, Taiwan*
[m] *University College, Korea University, Seoul 02481, South Korea*

ARTICLE INFO

Keywords:
Thermal enhancement
Latent heat storage system
Phase change materials (PCM)
Perforated fins
Multilayer perceptron
Genetic algorithm

ABSTRACT

The growing demand for sustainable and efficient energy systems has significantly increased the importance of latent heat storage systems (LHSSs) in renewable energy applications, particularly in solar thermal technologies. Despite the high energy storage density of PCMs, their inherently low thermal conductivity remains a major obstacle that limits charging performance and practical utilization. In the present study, a novel perforated fin-assisted LHSS is proposed and numerically investigated to enhance the charging performance of PCM-based storage systems. The effects of three key geometrical parameters, including perforation length (L), tube diameter (D), and storage body inclination angle (α), are systematically examined through a full factorial design approach. Furthermore, a multilayer perceptron neural network is established to estimate the system's thermal behavior, while genetic algorithm-based optimization identifies optimal configurations for short- and long-term heat absorption. The optimized short-term energy absorption design (*OSTE*) absorbs 7763 kJ during the short-term charging period. In contrast, the optimized long-term energy absorption design (*OLTE*) absorbs 7343 kJ, indicating that *OSTE* achieves approximately 5.72% higher short-term energy absorption than *OLTE*. Compared with the core design without perforated fins, which absorbs only 3077 kJ under the same conditions, the *OSTE* and *OLTE* configurations improve short-term energy absorption by approximately 152.3% and 138.6%, respectively. Under long-term operating conditions, *OLTE* absorbs 10,011 kJ, while *OSTE* absorbs 9957 kJ, corresponding to only 0.54% higher long-term energy absorption for *OLTE*. In contrast, the core design absorbs only 5395 kJ under the same conditions, demonstrating that *OLTE* and *OSTE* improve long-term energy absorption by approximately 85.6% and 84.6%, respectively. The results reveal that *OSTE*'s superiority during most stages of the charging process is substantially greater than *OLTE*'s slight long-term advantage. The findings

* Corresponding authors.
** Corresponding author at: College of Engineering and Architecture, Gulf University for Science and Technology, Mishref, Kuwait.
E-mail addresses: mkalmutairy@pnu.edu.sa (M. Al-Mutiry), medarbi@iu.edu.sa (M.A. Khlifi), Hhabuznadah@uj.edu.sa (H. Abu-Zinadah), chuan.nguyen@ut.edu.vn (D.C. Nguyen), Ibmahariq@gmail.com (I. Mahariq).

https://doi.org/10.1016/j.icheatmasstransfer.2026.112469

Available online 8 September 2026

demonstrate the strong potential of combining perforated fin networks, machine learning prediction models, and optimization algorithms to develop high-performance LHSSs for renewable energy applications.

Nomenclature

C_p	specific heat (J·kg^{-1}·K^{-1})
D	HTF tube diameter (mm)
E_m	melting enhancement ratio (%)
F	latent enthalpy of melting (J·kg^{-1})
I	characteristic height (m)
L	perforation length)mm)
P	pressure (Pa)
Ra	Rayleigh number
S	source term
t	time (s)
T	temperature (K)
u	velocity in x direction (m·s^{-1})
v	velocity in y direction (m·s^{-1})
β	coefficient of thermal expansion (K^{-1})
μ	dynamic viscosity (kg·m^{-1}·s^{-1})
φ	liquid fraction
α	storage inclination angle (degree)

Abbreviations

LHSS	latent heat storage systems
MLP	multilayer perceptron
PCM	phase change material
RMSE	root mean square error
TES	thermal energy storage

1. Introduction

The contemporary energy landscape is no longer defined solely by how energy is produced, but increasingly by how effectively it is managed across time [1]. In modern grids, energy is often generated when it is least needed and demanded when it is least available, creating a persistent temporal imbalance that challenges system stability and efficiency [2]. For instance, solar energy peaks at midday, while residential and industrial demand typically surges in the evening [3]. Similarly, waste heat from industrial processes is frequently dissipated into the environment despite its significant energetic value [4]. This mismatch leads not only to energy losses but also to increased operational costs, reliance on auxiliary systems, and higher greenhouse gas emissions [5]. Consequently, the role of energy storage has evolved from a supportive component to a central pillar in enabling flexible, resilient, and sustainable energy infrastructures [6].

Among the various storage strategies developed to address this challenge, thermal energy storage (TES) systems offer a particularly compelling solution for applications where heat accounts for a major fraction of energy consumption [7]. TES technologies capture excess thermal energy during surplus periods and release it when required, decoupling energy generation from utilization [8]. These systems are generally categorized as sensible heat storage, latent heat storage, and thermochemical storage, each characterized by distinct storage mechanisms and performance attributes [9]. Sensible heat storage relies on temperature variation within a material, while latent heat storage exploits phase transitions to store energy at nearly constant temperatures [10]. Thermochemical storage, by contrast, involves reversible chemical reactions with high energy densities but often greater system complexity [11]. Among these, latent heat storage systems (LHSS) have attracted increasing attention because they can deliver higher storage densities and more stable thermal outputs than conventional sensible storage approaches, making them highly attractive for compact, efficient energy systems [12].

Phase change materials (PCMs) lie at the core of LHSS, offering a unique capability to absorb and release large quantities of thermal energy during phase transitions, typically between solid and liquid states [13]. This characteristic enables PCM-based systems to achieve significantly higher energy storage densities, often several times greater than sensible heat systems operating over comparable temperature ranges, while maintaining near-isothermal conditions during operation [14]. Such behavior is particularly advantageous in applications requiring precise thermal regulation, including solar energy systems, building thermal management, and electronic cooling [15]. Nevertheless, the major challenge restricting the widespread use of PCMs is their limited ability to transfer thermal energy efficiently. This bottleneck has motivated extensive research into performance enhancement techniques [16]. These include high-conductivity additives, cascaded or multi-PCM arrangements, and active methods such as forced convection or oscillatory flows [17]. While each strategy offers measurable improvements, it often introduces additional complexity, cost, or stability concerns [18].

Recent studies have further investigated different approaches to overcome the inherent limitations of PCMs and improve their applicability in LHSSs. Liu et al. [19] investigated the rheological behavior of multi-walled carbon nanotube-enhanced liquid paraffin nanofluids and showed that incorporating nanoparticles significantly affects the viscosity characteristics of PCM-based fluids. Their results revealed non-Newtonian shear-thinning behavior, where both temperature and nanoparticle concentration played important roles in determining the nanofluid's rheological response. Such findings highlight the importance of considering modified thermophysical properties when designing advanced PCM-based storage systems. Besides material enhancement approaches, recent investigations have focused on improving heat transfer through innovative geometrical configurations. Said et al. [20] developed novel wavy channel structures for a triplex-tube LHSS and evaluated their influence on PCM solidification performance. Their results showed that optimized wavy geometries can substantially accelerate heat recovery by increasing thermal interaction between the heat transfer fluid and PCM domain. Similarly, Bahlekeh et al. [21] numerically studied the optimization of annular fin parameters in a triple-tube latent heat storage system. They showed that fin number, location, and thickness significantly influence melting behavior, with optimized fin arrangements providing considerable reductions in charging time due to enhanced heat communication between the conductive structures and PCM.

The incorporation of heat transfer enhancement structures, such as fins, pin arrays, and other conductive protrusions, has emerged as a particularly effective and practically viable solution [22]. The underlying mechanism is both simple and powerful. By embedding conductive structures within the PCM domain, the effective heat-transfer area increases dramatically, creating highly conductive pathways that channel thermal energy deep into regions that would otherwise remain thermally isolated [23]. Instead of heat slowly diffusing through the PCM bulk, these extensions act as thermal bridges, rapidly distributing energy and initiating multiple melting fronts simultaneously [24]. This fundamentally alters the melting dynamics, shifting from a conduction-dominated, sluggish process to a more spatially uniform, accelerated phase transition, thereby significantly reducing charging time and enhancing overall system responsiveness [25]. Moreover, the geometry, orientation, and distribution of these extended surfaces introduce additional degrees of freedom, enabling precise control over thermal gradients and phase-front evolution [26].

In addition to conventional thermal enhancement techniques, recent studies have explored intelligent strategies and advanced fin architectures for improving PCM-based energy storage systems [27]. Homod et al. [28] proposed an artificial intelligence-assisted thermal energy management strategy by integrating deep reinforcement learning clustering with multi-stage PCM storage systems. Their results indicated that combining advanced PCM arrangements with intelligent control strategies can reduce energy consumption and improve storage efficiency in building applications. Furthermore, Wu et al. [29] investigated toothed fin configurations as an alternative to conventional fin structures and showed that these designs can enhance melting performance while requiring less fin material. Their findings showed that optimized toothed openings and spacing improve heat transfer while preserving a larger effective PCM volume. These studies confirm that both material-level modifications and geometry-based enhancements play essential roles in advancing PCM thermal storage technologies. Niketan et al. [30] examined an X-shaped fin-based shell-and-tube configuration integrated with nanoparticle-enhanced solid–solid PCMs. Their results showed that an advanced fin configuration with branched X-fins significantly improved heat transfer uniformity and reduced charging time. In addition, selecting copper as the fin material improved charging performance by about 10.81% compared to carbon steel, while incorporating 4% by volume of graphene nanoparticles led to a notable additional improvement in thermal response. Moreover, increasing the inner wall temperature from 498 K to 544 K (a 9.23% increase) resulted in a remarkable 96.65% reduction in charging time. Tang et al. [31] introduced a discontinuous fin design for a vertical storage unit to more effectively regulate the solidification process. Their numerical findings revealed that fin geometry plays a decisive role in controlling heat-release dynamics, with a critical main-fin length of 15 mm. Deviations below this value had minimal influence, whereas longer fins gradually degraded performance due to delayed heat extraction. Furthermore, the bifurcation angle exhibited an optimal range of 0.45–0.6, within which the system achieved the fastest solidification. Under optimized conditions ($L1 = 15$ mm and $\alpha = 0.45$), the proposed configuration reduced total solidification time by 22.14% and increased the heat release rate by 28.45% compared to conventional longitudinal fin designs. Mao et al. [32] proposed a triangular-rib-based configuration to analyze its melting behavior under varying design and operating conditions. The enhanced system achieved complete melting in less than 5 h, whereas the conventional configuration achieved only 48% melting in the same period. Furthermore, the selected configurations increased thermal energy storage capacity by nearly 75% and reduced the economic payback period by approximately 13.4%. Alnakeeb et al. [33] analyzed the effect of tube arrangement and orientation in a system employing elliptic channels while maintaining a constant heat transfer area. Their results indicated a strong dependence of melting behavior on flow-induced convection patterns. Specifically, the configuration with four vertically oriented tubes in a vertical array achieved the highest melting rate of 0.0175 kg/min. In contrast, a horizontal arrangement with three horizontally oriented tubes resulted in a significantly lower rate of 0.00785 kg/min. This represents more than a twofold enhancement in melting performance due solely to geometric orientation. The superior performance of vertical configurations was attributed to the intensified natural convection currents, which effectively augment heat transport within the PCM and accelerate the phase transition process. Deng et al. [34] proposed a modular multi-section system composed of dome-shaped units, where each dome wall functions as an independent heat transfer channel, removing the requirement for internal fins. The optimized configurations showed substantial improvements over the baseline design; one configuration achieved approximately 21,980 kJ of stored energy in 5 h, about 222% higher than the reference case, while capturing nearly 99.7% of this energy within the first 170 min. Another configuration reached a maximum energy storage of 23,495 kJ over the same duration, corresponding to a 115% enhancement. Additionally, a balanced design selected through multi-criteria decision analysis achieved improvements of about 207% and 105% in energy absorption over 3 and 5 h, respectively.

In parallel with these physical enhancement strategies, the methodological approach to analyzing LHSS has undergone a notable transformation [35]. Traditionally, researchers have investigated the performance of such systems through detailed numerical simulations or carefully controlled experimental studies, both of which, while accurate, are often time-intensive and computationally demanding when dealing with large parametric spaces [36]. In recent years, data-driven modeling techniques, particularly artificial neural networks such as multilayer perceptrons (MLPs), have gained prominence as efficient predictive tools [37]. These models learn the complex, nonlinear relationships between input parameters (e.g., geometric features, material properties, and operating conditions) and system responses, effectively creating a fast, reliable surrogate for high-fidelity simulations [38]. Rather than repeatedly solving governing equations, a well-trained MLP can predict system behavior almost instantaneously with remarkable accuracy [39]. This shift enables researchers to explore vast design spaces, identify optimal configurations, and perform sensitivity analyses with unprecedented speed [40]. In essence, neural networks transform the problem from repeated physical computation into intelligent inference, opening new pathways for rapid design and optimization of advanced LHSSs [41].

Mahboobtosi et al. [42] explored data-driven modeling to analyze the solidification behavior of PCM systems enhanced with vascular-inspired fin structures and advanced hybrid nanofluids. In their work, they developed an MLP to accurately predict key thermal performance indicators, including solid fraction, average temperature, and total stored energy. The study showed that variations in radiative heat transfer significantly influence system dynamics: increasing the radiation parameter notably accelerated solidification while slightly reducing average temperature and stored energy. Zhao et al. [43] introduced a hybrid modeling framework to improve state estimation in LHSSs under practical operating constraints. Their approach integrates a physics-informed neural network for temperature field reconstruction with an MLP dedicated to state-of-charge prediction, forming a unified physics-informed state estimator. By embedding governing physical principles directly into the learning process, the model effectively overcomes common limitations of purely data-driven approaches, particularly in situations with limited training data. The proposed framework demonstrated high predictive accuracy, achieving very low errors in both temperature estimation and state-of-charge evaluation. Moreover, the study highlighted the model's robustness to variations in sampling intervals and showed that an appropriately designed network architecture can balance accuracy and generalization. Khalid et al. [44] examined enhancing an LHSS through the combined use of nanoparticle-enriched PCMs and optimized fin geometries, alongside data-driven prediction techniques. In their study, they modified paraffin wax with nanoparticles to improve thermal conductivity and numerically analyzed a triplex-tube unit equipped with V-shaped fins using the enthalpy–porosity method. To complement the numerical approach, an MLP model was developed for rapid prediction of thermophysical behavior, achieving high accuracy with a coefficient of determination exceeding 0.998 and a mean square error below 1.5×10^{-3}. The results demonstrated that geometric configuration plays a critical role in melting performance; specifically, selected fin arrangements enabled more than 98% of the PCM to melt within 3600 s, whereas less favorable designs resulted in only 84.86% melting over the same period.

Although considerable efforts have been devoted to improving the thermal response of PCM-based LHSSs through fin structures, advanced materials, and optimization techniques, several challenges remain. Conventional fin-assisted designs generally enhance heat conduction; however, excessive fin integration may reduce the effective PCM volume and restrict natural convection within the storage domain. Moreover, most previous studies have focused on optimizing individual design parameters, while simultaneous consideration of thermal enhancement, structural integration, and rapid performance prediction remains limited. Therefore, innovative storage architectures are still needed that can provide enhanced heat transfer while maintaining high storage capacity and operational flexibility. To address this research gap, the present study proposes a novel perforated fin-assisted LHSS in which an interconnected fin network is integrated around the HTF tubes. The proposed design simultaneously improves conductive heat transfer through extended thermal pathways and promotes natural convection through strategically distributed perforations. Structurally, the interconnected fin network acts as a supporting framework that firmly stabilizes the HTF tubes in the storage body. The proposed architecture also offers remarkable material flexibility. The interconnected fin framework provides a general thermal platform that can accommodate various PCMs with different melting temperatures and thermophysical properties. This characteristic significantly broadens the system's applicability to diverse thermal management requirements. In addition, a machine learning-based prediction framework using a multilayer perceptron (MLP) model is developed to rapidly estimate the system's thermal performance, while a combined genetic algorithm (GA) and TOPSIS approach identifies optimal configurations. The main objective of this work is to develop and evaluate an efficient PCM-based thermal storage architecture that achieves accelerated charging performance while maintaining effective energy storage capacity. The outcomes of this study provide new insights into the design and optimization of advanced latent heat storage systems for renewable energy and thermal management applications.

2. System description and material properties

2.1. Integration with a solar thermal application

Fig. 1 illustrates the practical implementation of an LHSS within a solar thermal application. The system is designed to operate as an intermediate thermal management unit between the solar collector and the domestic hot water tank, enabling efficient storage and redistribution of thermal energy under fluctuating operating conditions. After gaining heat from the solar collector, the HTF flows into the thermal storage unit and releases its energy to the PCM. The PCM then stores thermal energy as latent heat during melting. The thermal storage unit acts as an energy buffer that decouples heat generation from heat utilization. During high-solar-radiation periods, hot HTF enters the storage unit and transfers thermal energy to the PCM domain. Once thermal demand arises, the stored energy can be recovered and utilized to support domestic heating applications. The directional arrows presented in the figure indicate the HTF circulation path throughout the system during operation.

2.2. Geometrical design of the proposed LHSS

The thermal storage system integrated within the solar-assisted application shown in Fig. 1 is systematically developed and geometrically detailed in Fig. 2. Fig. 2(a) presents the 3D view of the introduced LHSS equipped with removable upper and lower covers. These covers provide easy access to the internal storage unit for assembly, maintenance, and replacement. Fig. 2 (b) illustrates the internal geometrical configuration of the storage unit. It contains multiple HTF tubes embedded within the PCM domain to transfer thermal energy directly into the storage medium. Surrounding the HTF tubes, an interconnected perforated fin network is introduced to improve thermal transport and mechanical stability simultaneously. The fin structure extends throughout the complete PCM storage region and surrounds the HTF tubes over the full length of the thermal storage unit. This continuous arrangement was considered to provide uniform thermal pathways along the storage domain and maintain consistent mechanical support for the internal tube arrangement. Besides, the present design incorporates strategically distributed perforations within the fin network. They reduce flow obstruction and promote buoyancy-driven motion of the molten PCM. In Fig. 2, the PCM region has a total length of 500 mm.

2.3. Thermophysical properties of the applied materials

The present LHSS employs RT50 as the phase change material because of its favorable thermal characteristics for medium-temperature latent heat storage applications. Specifically, RT50 has a melting temperature range of 318.15–324.15 K and a latent heat of 168 kJ/kg, which enables the storage and release of a considerable amount of thermal energy within a relatively narrow temperature interval. This characteristic is particularly advantageous for thermal energy storage applications because it allows a large amount of energy to be stored through phase change while keeping the PCM temperature within a limited range. In addition, the relatively stable thermo-physical behavior of RT50 during repeated melting and solidification cycles makes it suitable for cyclic thermal storage applications. Its melting temperature range is also compatible with the operating temperature considered in the present solar-assisted thermal storage system, making RT50 a suitable PCM for medium-temperature solar thermal energy

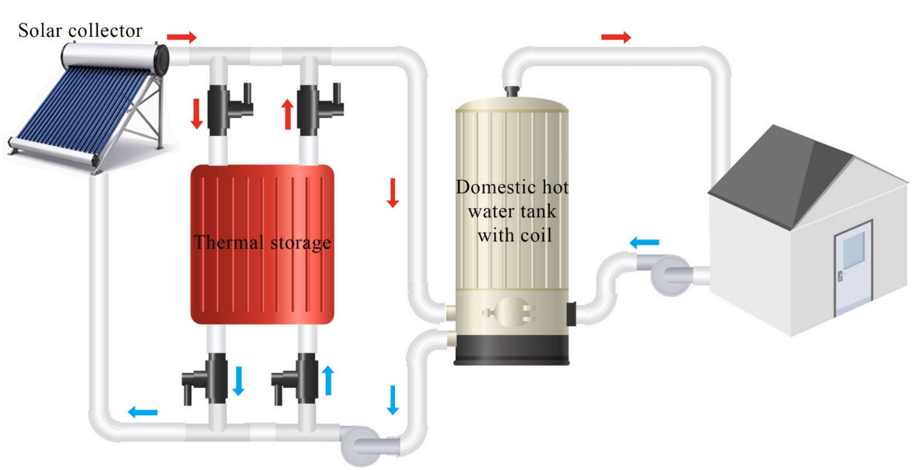

Fig. 1. Schematic representation of a thermal storage system integrated with a solar-assisted domestic hot water application.

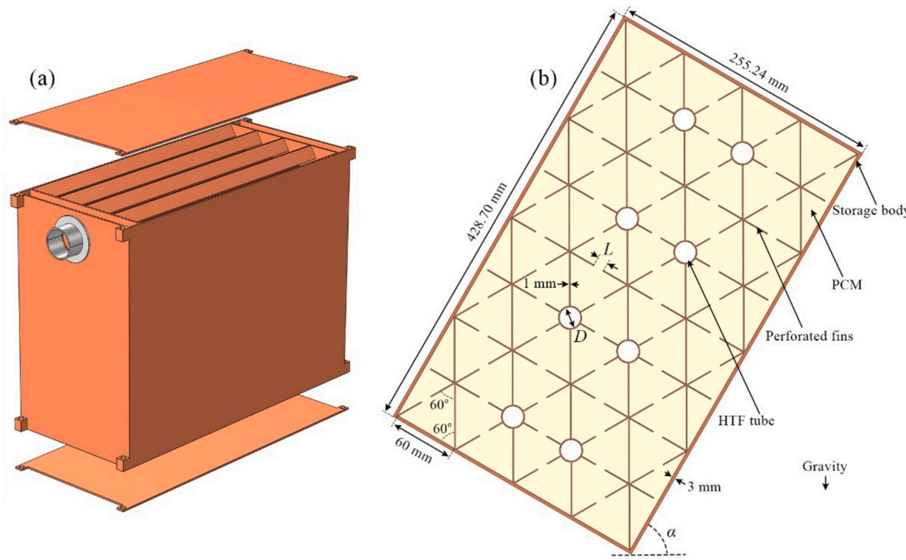

Fig. 2. (a) 3D representation of the proposed LHSS with removable upper and lower covers, and (b) geometrical details of the PCM storage unit incorporating HTF tubes and perforated fin network.

storage and domestic heating applications. For the solid structures, including the storage body, HTF tubes, and the perforated fin network, copper is selected for its excellent thermal conductivity. Copper's high conductivity substantially improves thermal uniformity throughout the storage unit. In addition, copper provides favorable mechanical strength and structural durability, which are essential for maintaining the integrity of the modular fin-supported architecture during long-term operation. Table 1 summarizes the thermo-physical properties of RT50 and copper used in the numerical simulations.

3. Mathematical formulation and physical modeling

3.1. Phase change modeling via enthalpy–porosity framework

The PCM charging process is implicitly incorporated via the enthalpy-porosity approach, which circumvents explicit interface tracking while preserving thermodynamic consistency. The phase evolution is represented by a continuous liquid-fraction field that quantifies the proportion of material in the liquid state and governs local latent-heat storage. The intermediate region between solid and liquid phases forms the mushy zone, where both conductive and convective heat transfer mechanisms coexist. In the mentioned zone, the PCM is treated as a pseudo-porous medium, and its flow characteristics are gradually suppressed as the solidification proceeds. The mushy-zone constant governs the strength of this suppression and is important for stabilizing the numerical solution and preventing non-physical velocity penetration into solid regions. Furthermore, buoyancy-driven flow in the liquid phase is resolved using the Boussinesq approximation, allowing temperature-induced density changes to drive natural convection. This integrated formulation enables a consistent coupling between heat transfer and fluid flow, capturing the shift from conduction-dominated behavior at early stages to convection-enhanced transport during melting.

Table 1
Thermo-physical properties of the PCM and solid materials employed in the present study.

Material properties	RT50 [24]		Copper [45]
	Solid	Liquid	
ρ (kg·m^{-3})	880	760	8960
k (W·m^{-1}·K^{-1})	0.2	0.2	386
C_p (J·kg^{-1}·K^{-1})	2000	2000	383
μ (kg·m^{-1}·s^{-1})	–	0.0038	–
β (K^{-1})	0.0006		–
F (J·kg^{-1})	168,000		–
T_m (K)	318.15–324.15		–

3.2. Model simplification and underlying assumptions

The simplifying assumptions are grouped into four categories to reduce computational complexity and maintain the dominant heat transfer physics:

- Body forces and gravity effects: A gravitational field with an acceleration of 9.81 m/s^2 was imposed along the negative vertical axis, thereby driving natural convection currents during PCM melting.
- Flow regime and dimensionality: The physical model is developed in a 2D, transient framework to capture coupled heat transfer and fluid-flow phenomena during the energy-absorption process. The fluid is assumed to be incompressible. The molten PCM flow is considered to remain laminar, justified by a Rayleigh number below 10^9 [46].
- Material properties and phase behavior: All materials are assumed isotropic and homogeneous throughout the computational domain. The thermo-physical properties of the employed materials are considered constant within each phase to simplify the simulation process (Table 1). Nevertheless, density variations in the liquid PCM are accounted for utilizing the Boussinesq approximation, allowing buoyancy-driven flow to be accurately represented without introducing full compressibility effects.
- Heat transfer simplifications: Viscous dissipation is neglected due to its negligible contribution relative to conductive and convective mechanisms under the considered operating conditions.

3.3. Principal equations of the system

The thermofluid characteristics of the proposed LHSS are governed by the coupled conservation equations of mass, momentum, and energy. These equations are solved simultaneously to capture the interaction between heat transfer, fluid motion, and phase transition. Eq. (1) represents the Rayleigh number (Ra), which indicates the intensity of natural convection generated by temperature-induced density variations [47].

$$Ra = \frac{g\beta C_p \rho^2 (T_{HTF} - T_{PCM}) l^3}{\mu k} \tag{1}$$

Eq. (2) corresponds to the continuity equation, which expresses the conservation of mass within the liquid PCM domain. This equation ensures that the net mass entering and leaving any differential control volume remains balanced during fluid motion. Since the PCM is assumed incompressible, the divergence of velocity becomes zero [48].

$$\frac{\partial u}{\partial x} + \frac{\partial v}{\partial y} = 0 \tag{2}$$

Eqs. (3) and (4) describe the momentum conservation equations in the horizontal (x) and vertical (y) directions, respectively. These equations are derived from the Navier–Stokes formulation and account for inertial forces, pressure gradients, viscous diffusion, and velocity suppression within the mushy region. In the vertical momentum equation, the buoyancy term introduced by the Boussinesq approximation drives natural convection in the molten PCM. The source terms S_x and S_y are associated with the enthalpy–porosity method and gradually damp fluid motion as the PCM solidifies [49].

$$\rho_{0,l}\left(\frac{\partial u}{\partial t} + u\frac{\partial u}{\partial x} + v\frac{\partial u}{\partial y}\right) = -\frac{\partial P}{\partial x} + \mu\left(\frac{\partial^2 u}{\partial x^2} + \frac{\partial^2 u}{\partial y^2}\right) + S_x \tag{3}$$

$$\rho_{0,l}\left(\frac{\partial v}{\partial t} + u\frac{\partial v}{\partial x} + v\frac{\partial v}{\partial y}\right) = -\frac{\partial P}{\partial y} + \mu\left(\frac{\partial^2 v}{\partial x^2} + \frac{\partial^2 v}{\partial y^2}\right) + g\rho_{0,l}(1 - \beta(T - T_0)) + S_y \tag{4}$$

In Eq. (4), T_0 corresponds to the initial temperature of the PCM before the charging process begins. Eq. (5) is the energy conservation equation for the PCM region. This equation governs the combined transport of sensible and latent heat during melting. The left-hand side represents transient and convective heat transport, while the right-hand side describes conductive heat diffusion [50].

$$\rho_{0,l}\left(\frac{\partial H}{\partial t} + u\frac{\partial H}{\partial x} + v\frac{\partial H}{\partial y}\right) = k_l\left(\frac{\partial^2 T}{\partial x^2} + \frac{\partial^2 T}{\partial y^2}\right) \tag{5}$$

Eq. (6) represents the heat conduction equation within the solid regions, including the storage body, HTF tubes, and perforated fin network. Since no fluid motion occurs within these solid components, heat transfer occurs solely by conduction [51].

$$\rho_s C_{P,s}\frac{\partial T}{\partial t} = k_s\left(\frac{\partial^2 T}{\partial x^2} + \frac{\partial^2 T}{\partial y^2}\right) \tag{6}$$

Eq. (7) defines the total enthalpy (H) as the summation of sensible enthalpy (h) and latent heat contribution (ΔH). This formulation enables continuous modeling of phase change without explicitly tracking the solid–liquid interface [52].

$$H = h + \Delta H \tag{7}$$

Eq. (8) expresses the sensible enthalpy formulation, where the temperature-dependent thermal energy is calculated relative to a reference state [53].

$$h = h_{ref} + \int_{T_{ref}}^{T} C_p dT \tag{8}$$

Eq. (9) quantifies the portion of energy stored as latent heat within the PCM. Here, ΔH represents the thermal energy absorbed or released due to phase change, φ is the local liquid fraction, and F denotes the total latent heat content of the material. Physically, it links the phase evolution to energy storage, meaning that only the fraction of PCM that has melted contributes to latent energy accumulation [54].

$$\Delta H = \varphi F \tag{9}$$

The piecewise relation in Eq. (10) defines the PCM's phase state as a function of temperature. When the PCM temperature is below the solidus temperature, it is fully solid ($\varphi = 0$). Between the solidus (T_s) and liquidus (T_l) temperatures, the PCM exists in a mushy zone, where it is partially liquid. The fraction is linearly interpolated to ensure a smooth transition. Above T_l, the PCM is fully liquid ($\varphi = 1$). This formulation is central to the enthalpy–porosity method, allowing the model to capture continuous melting without explicitly tracking interfaces [55].

$$\varphi = \begin{cases} 0 & \text{if} \quad T_{PCM} < T_s \\ \dfrac{T_{PCM} - T_s}{T_l - T_s} & \text{if} \quad T_s \le T_{PCM} \le T_l \\ 1 & \text{if} \quad T_{PCM} > T_l \end{cases} \tag{10}$$

Eqs. (11) and (12) show the source terms that are added to the momentum equations to suppress fluid motion in partially solid regions. u and v are velocity components in the x- and y-directions. $A(\varphi)$ is a damping coefficient that depends on the local liquid fraction. Physically, these equations simulate the resistance imposed by solidifying PCM, ensuring that the velocity decreases smoothly as the PCM transitions from liquid to solid. This prevents unrealistic penetration of fluid motion into solid regions and stabilizes the numerical solution [56].

$$S_x = -A(\varphi)u \tag{11}$$

$$S_y = -A(\varphi)v \tag{12}$$

In Eq. (13), $A(\varphi)$ determines how strongly the mushy zone suppresses fluid motion. M_f is the mushy zone constant controlling the maximum damping strength. The numerator $(1 - \varphi)^2$ ensures that damping is strongest when the PCM is mostly solid. The denominator $\varphi^3 + \varepsilon$ prevents numerical singularities and ensures that damping reduces rapidly as the PCM melts ($\varphi \to 1$). In essence, this equation provides a smooth transition from solid-like to liquid-like behavior, enabling accurate modeling of convective flow within the molten PCM while accounting for partially solid regions [57].

$$A(\varphi) = M_f\frac{(1-\varphi)^2}{\varphi^3 + \varepsilon} \tag{13}$$

The melting enhancement ratio (E_m) in Eq. (14) quantifies the increase in PCM charging performance resulting from fin incorporation. φ is the local liquid fraction in the system with fins. φ_{cd} is the corresponding fraction in a core design (finless) configuration. By expressing the difference as a percentage, E_m indicates how much faster or more effective the melting process is with the fin network. Positive E_m values represent enhanced heat transfer and accelerated phase change, directly linking the fin design to thermal performance [58].

$$E_m = \left[\frac{\varphi}{\varphi_{cd}} - 1\right] \times 100\% \tag{14}$$

3.4. Initial and boundary condition specification

To accurately simulate the PCM charging process, initial and boundary conditions are specified to ensure numerical stability and physical consistency:

- All solid boundaries, including the walls of the containment, HTF tubes, and fin surfaces, enforce a no-slip condition ($u = v = 0$), which ensures that the fluid velocity at the solid interface is zero. Simultaneously, a no-temperature-jump condition is applied, maintaining thermal continuity between solid surfaces and the adjacent PCM.
- The system is assumed to operate at atmospheric pressure ($P = 1$ atm) both inside the LHSS and in the ambient domain. This simplifies the momentum formulation by maintaining incompressibility and removing the need for pressure-driven boundary modifications.
- The enclosure boundaries were considered under an isothermal condition with a prescribed temperature of 333.15 K, depicting the

thermal boundary provided by the HTF. The PCM and solid parts are uniformly initialized at 298.15 K.
- The thermal storage unit is designed and numerically evaluated under well-insulated operating conditions. Accordingly, adiabatic boundary conditions are applied to the enclosure's external surfaces, assuming negligible heat exchange between the storage unit and the surrounding environment.

3.5. Numerical methodology and solution procedure

The present LHSS was numerically studied utilizing the commercial computational fluid dynamics (CFD) software ANSYS Fluent. It provides a robust framework for handling coupled thermo-fluid problems and has been extensively validated for phase change simulations in thermal energy storage applications. To solve the governing equations, the computational domain was discretized into a large number of finite control volumes through the finite volume method (FVM). The convective terms appearing in the momentum and energy equations were discretized using a second-order upwind scheme. Compared with first-order discretization methods, the second-order approach provides higher numerical accuracy. Since the liquid PCM is treated as an incompressible fluid, the pressure and velocity fields are strongly coupled through the continuity equation. To establish this coupling, the Semi-Implicit Method for Pressure-Linked Equations (SIMPLE) algorithm was employed. The SIMPLE scheme iteratively corrects the pressure and velocity distributions until mass conservation is satisfied throughout the computational domain.

For pressure interpolation at the cell faces, the Pressure Staggering Option (PRESTO) scheme was adopted. The PRESTO formulation is particularly suitable for buoyancy-dominated flows because it improves pressure-field accuracy in regions with strong natural convection. To ensure numerical stability during the iterative solution procedure, appropriate under-relaxation factors were specified for the governing variables. The under-relaxation factor for pressure was set to 0.3 to maintain stable pressure correction behavior, while a value of 0.7 was assigned for the momentum equations to achieve balanced velocity convergence. For the liquid-fraction equation associated with the phase change process, a higher relaxation factor of 0.9 was used to accelerate convergence of the melting field. In contrast, the energy and density equations were solved with a full relaxation value of 1.0 to preserve thermal accuracy during the transient simulation. The iterative calculations were continued until convergence was achieved for all governing equations. Convergence was monitored through normalized residuals of the continuity, momentum, and energy equations, and the solution was considered converged when all residuals decreased below 10^{-5}. This strict convergence criterion ensures high numerical precision and guarantees the physical reliability of the obtained thermal and flow predictions.

4. Numerical validation and assessment of the 2D modeling approach

Before conducting the detailed parametric analysis, the numerical model used in this study was validated against the experimental study by Kousha et al. [59]. In their experimental study, the HTF volumetric flow rate was reported as 0.4 L/min for each tube. In the present work, the LHSS is primarily analyzed using a 2D computational model. This simplification is physically justified because the HTF temperature variation along the storage unit's longitudinal direction remains very limited during operation. Once the HTF flow rate reaches a sufficiently high level, axial thermal variations become insignificant, with the temperature difference generally limited to values below 0.5 K, indicating that the dominant thermal gradients occur mainly in the transverse direction rather than along the flow path. Consequently, heat transfer and melting behavior can be accurately represented using a 2D formulation, thereby significantly reducing computational cost and simulation time. Nevertheless, to ensure that the 2D assumption does not compromise the physical accuracy of the obtained results, an additional 3D simulation was also performed under the same operating conditions. The results from both the 2D and 3D numerical models were then compared with the experimental data of Kousha et al. [60] to assess the reliability of the adopted simplification. In all validation simulations, the mushy zone constant was fixed at 10^6, which stably suppressed non-physical velocities within the solidifying PCM regions while preserving numerical convergence. To evaluate the influence of the mushy zone constant on the numerical predictions, we performed an additional sensitivity analysis by varying this parameter between 10^5, 10^6, and 10^7. As illustrated in Fig. 3(a), reducing the mushy zone constant to 10^5 slightly accelerates melting because weaker momentum damping within the mushy region enhances buoyancy-driven convection and thermal transport. Conversely, larger values increase the resistance against fluid motion and slightly delay melting. Nevertheless, the results obtained using 10^6 and 10^7 show similar trends, demonstrating that this parameter's influence decreases at higher values. Furthermore, after complete melting, all cases converge because the mushy-zone resistance vanishes in the fully liquid PCM region. Given the excellent agreement with experimental measurements and its widespread use in previous PCM studies, 106 was selected as the mushy-zone constant for all subsequent simulations.

Fig. 3(a) presents the average PCM temperature obtained from the experimental measurements, the 2D simulation, and the 3D simulation. Both numerical approaches show excellent agreement with the experimental data throughout the charging process. The numerical predictions successfully capture the thermal behavior and closely reproduce the experimental trend. A detailed comparison further indicates that the discrepancy between the 2D and 3D simulations is very limited. The predicted temperature profiles from both models remain nearly overlapping throughout most of the charging period, confirming that axial thermal variations have a negligible impact on the storage unit's performance. Moreover, the 2D model shows slightly better agreement with the experimental data at certain stages, while maintaining substantially lower computational demand than the full 3D simulation. These observations validate the suitability of the 2D approach for the present investigation. To further verify the physical accuracy of the numerical model, the numerically obtained melting patterns were visually compared with the experimental observations, as shown in Fig. 3(b). The figure illustrates the solid–liquid interface at different charging times. Strong similarity can be observed between the experimentally captured melting fronts and the numerically predicted ones.

5. Grid independence test

A systematic grid-refinement study is conducted to ensure that the mesh resolution does not influence the solution. Table 2 summarizes the results of this analysis. A non-uniform quadrilateral grid divides the simulation domain. Additionally, a boundary-layer mesh is applied adjacent to solid boundaries to capture sharp variations in temperature and velocity near the walls. Grid reliability is verified by maintaining skewness below 0.31, indicating a well-shaped element distribution suitable for accurate flow and heat transfer simulations. Four different mesh densities, ranging from 58,120 to 989,677 elements, are tested. The average change in liquid fraction relative to the previous mesh is used as the convergence criterion. As shown in Table 2, refinement beyond approximately 490,025 elements produces negligible variation in liquid fraction (less than 1%), while further mesh densification significantly increases computational time. Based on this analysis, the mesh with 490,025 elements is selected for all subsequent simulations.

6. Time-step independence test

In addition to spatial discretization, the influence of temporal resolution on the simulation results is evaluated through a time-step

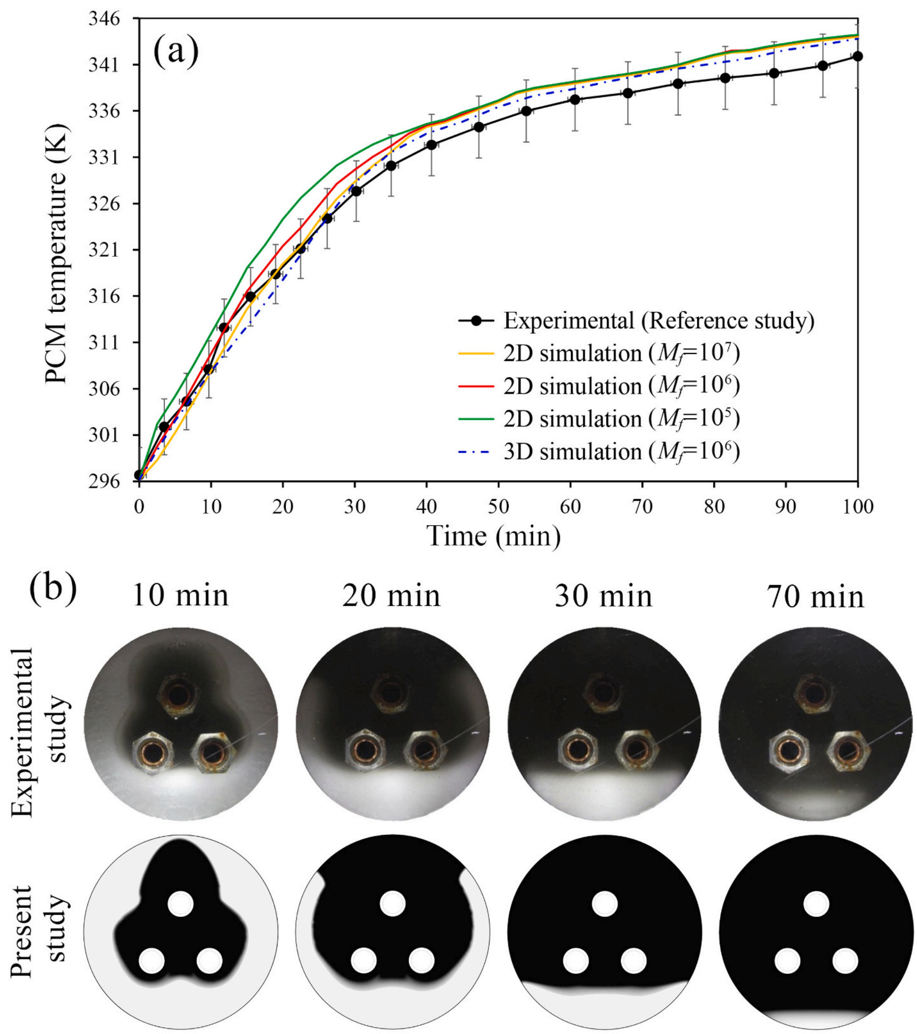

Fig. 3. Validation of the present numerical model against the experimental study of Kousha et al. [59]: (a) comparison of PCM temperature evolution obtained from experimental measurements, present 2D simulations under different mushy zone constants, and present 3D simulations, and (b) comparison of melting front evolution and phase distribution at different charging times.

Table 2
Grid independence analysis for the PCM charging simulation, showing the average change in liquid fraction and computational time for varying mesh densities.

Number of mesh elements	Average change in liquid fraction relative to previous mesh (%)	Computational time (h)
58,120	–	0.8
119,010	10.220	2.2
490,025	5.316	8.0
989,677	0.852	16.5

Table 3
Time-step independence study for the PCM charging process, presenting the average variation in liquid fraction and corresponding computational cost for different temporal resolutions.

Time-step	Average change in liquid fraction relative to previous time-step (%)	Computational time (h)
1	–	1.0
0.5	7.159	1.9
0.1	3.888	8.0
0.05	0.550	15.3

independence study, summarized in Table 3. The average change in liquid fraction relative to the previous time step is used to assess convergence with respect to temporal discretization. Four different time steps, ranging from 1 s to 0.05 s, are investigated. Larger time steps speed up simulations but can introduce significant temporal discretization errors. Excessively small steps increase computational demand while providing negligible gains in solution accuracy. As shown in Table 3, the average variation in the liquid fraction decreases substantially as the time step decreases. A time step of 0.1 s is chosen to achieve accurate results with deviations below 4% relative to the finer step while maintaining reasonable computational efficiency. Smaller time steps, such as 0.05 s, offer only a marginal improvement (<0.6%) at the expense of a significant increase in CPU time. Therefore, 0.1 s is adopted for all subsequent simulations to ensure reliable yet efficient predictions of the PCM melting process.

7. Machine learning-based prediction and multi-objective optimization framework

7.1. Development of the MLP prediction model

To accelerate analysis and prediction of the thermal behavior of the proposed LHSS, an MLP model was developed in this study. The objective of the MLP framework is to establish an accurate relationship between the geometrical design parameters and the thermal performance indicators of the storage system. Fig. 4 (a) illustrates the overall procedure adopted to construct the MLP model. The multilayer perceptron (MLP) model developed in this study was implemented using the MATLAB Feedforward Network (feedforwardnet) tool. The feedforward neural network was trained using the back-propagation learning algorithm, which iteratively updates the connection weights and biases by minimizing the difference between the predicted and numerical responses. The developed network follows a conventional feedforward architecture consisting of three sequential components: an input layer, one hidden layer, and an output layer. The input layer contains the geometrical design parameters of the latent heat storage system, including perforation length (L), HTF tube diameter (D), and storage body inclination angle (α). These parameters were previously illustrated in Fig. 2(b). The hidden layer extracts nonlinear relationships between the input variables and thermal responses. In contrast, the output layer provides the predicted thermal performance indicators, including short-term energy absorption (*STE*) and long-term energy absorption (*LTE*). The dataset used to train and evaluate the MLP model was generated using a full-factorial design of experiments. Three variables were considered (each at three levels), resulting in $3^3 = 27$ different design configurations. Table 4 summarizes the variables and corresponding levels used in the full factorial method, where the first, second, and third levels correspond to coded values of -1, 0, and $+1$, respectively. This approach enables systematic coverage of the entire investigated design space rather than selecting data points arbitrarily. Therefore, the obtained 27 datasets represent all possible combinations of the selected input parameters within the considered parameter ranges and provide a reliable basis for developing the predictive model.

Due to the limited number of available datasets, careful consideration was given to data division and model validation. The 27 available datasets were randomly divided into training and unseen datasets, with 70% of the data assigned for model training and the remaining 30% reserved for independent evaluation of the developed model. Random allocation was used to prevent bias caused by the dataset's ordering. Moreover, because a small dataset may cause prediction accuracy to depend on the selected data partition, K-fold cross-validation was also performed. This method is particularly suitable for limited datasets because it repeatedly changes the training and testing subsets and evaluates whether the obtained model performance remains consistent regardless of the data division. As shown in Fig. 4(a), the network development procedure included initialization of weights and biases. This study employed the Levenberg–Marquardt (LM) algorithm to train the MLP model. The LM algorithm was selected for its fast convergence and strong performance in nonlinear regression problems, making it suitable for training the MLP model used to predict the thermal performance indicators of the proposed LHSS. During training, the LM algorithm iteratively updated the network weights and biases by minimizing the prediction error between the numerical simulation results and the MLP outputs. The final network performance was evaluated using several statistical indicators, including root mean square error (RMSE) and the coefficient of determination (R^2) [60]. Fig. 4 (b) presents the general structure of the developed MLP model

Table 4
Design factors and levels employed in the full factorial design methodology.

Design factors	Factor levels		
	-1	0	$+1$
L (mm)	5	10	15
D (mm)	10	20	30
α (degree)	60	90	120

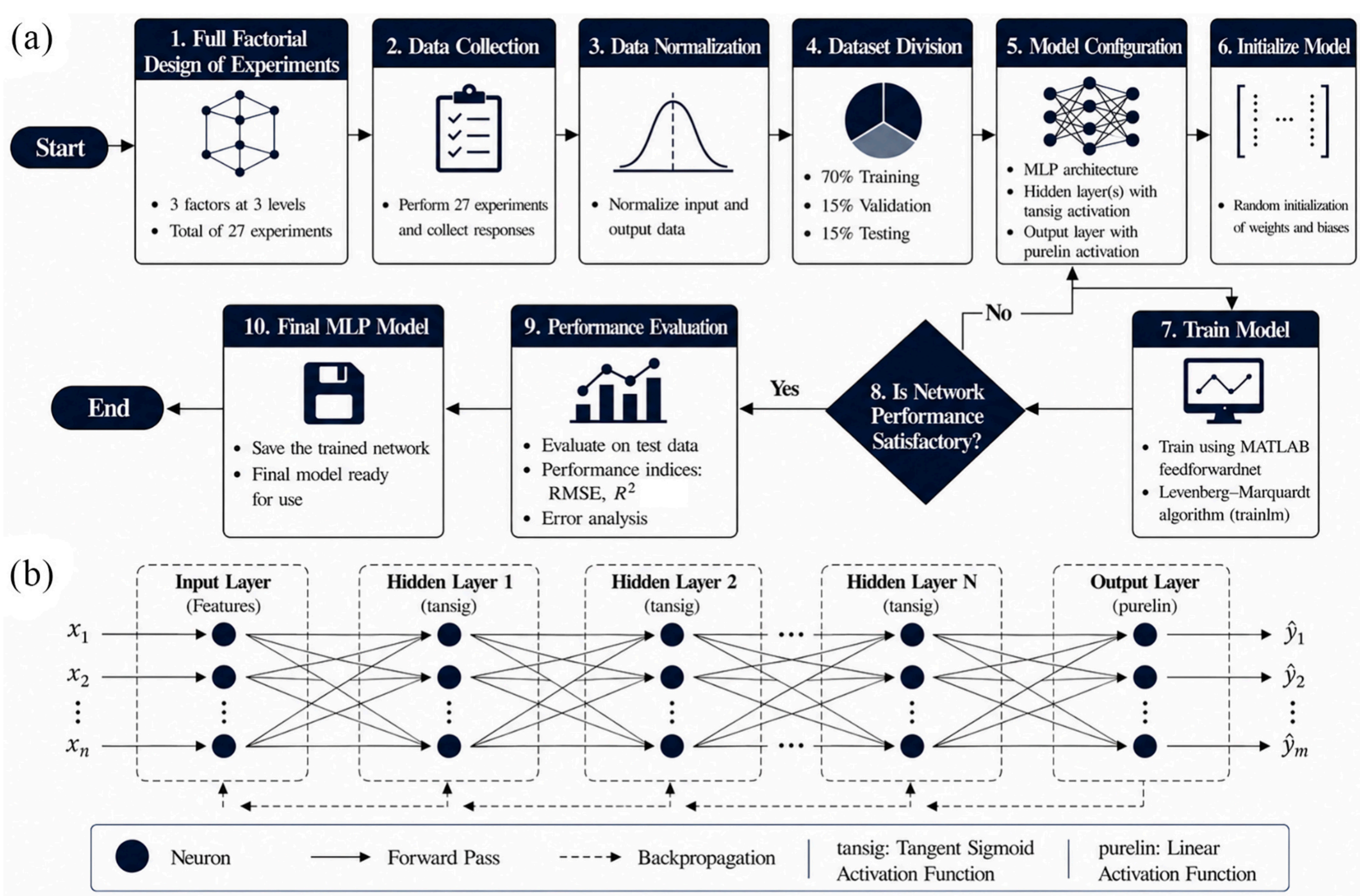

Fig. 4. (a) Workflow of the MLP model development and training procedure, and (b) schematic representation of the feedforward neural network architecture employed in the present study.

schematically.

$$RMSE = \sqrt{\frac{\sum_{i=1}^{m}\left(r_{pred}\text{-}r_{num}\right)^2}{m}} \tag{15}$$

$$R^2 = 1\text{-}\frac{\sum_{i=1}^{m}\left(r_{num}\text{-}r_{pred}\right)^2}{\sum_{i=1}^{m}\left(r_{num}\text{-}\overline{r_{pred}}\right)^2} \tag{16}$$

7.2. GA-based optimization

The developed MLP prediction model was coupled with the GA optimizer to rapidly evaluate large numbers of candidate configurations without repeatedly performing computationally expensive numerical simulations. The optimization process used the geometrical design variables. The GA used stochastic uniform selection as its selection operator. This method was selected because it provides a balanced mechanism for choosing parent solutions by assigning selection probabilities proportional to their fitness values while maintaining population diversity. As a result, highly suitable solutions have a greater probability of contributing to the next generation. In contrast, less dominant solutions still retain a chance of being selected, helping prevent premature convergence. The GA was configured using a population size of 1000 individuals to ensure broad exploration of the design space. An elite count of 50 was used to preserve the best-performing solutions across generations and prevent the loss of highly favorable designs. In addition, the mutation probability and crossover probability were set to 0.01 and 0.8, respectively. The crossover operation enables information exchange between parent solutions to generate potentially superior offspring, whereas mutation introduces random variation that helps avoid premature convergence and enhances global search. The optimization procedure was continued for up to 300 generations to ensure sufficient convergence toward the optimal solution.

Initially, the optimization analysis was performed separately using single-objective optimization. The first optimization target focused on maximizing the system's short-term energy absorption capability. The second objective aimed to maximize long-term energy absorption. Although single-objective optimization provides useful insight into the influence of design variables, optimizing one performance indicator independently may negatively affect another competing objective. Therefore, this study extends beyond conventional single-objective approaches by performing a multi-objective optimization analysis that considers both short- and long-term energy absorption characteristics simultaneously. This approach enables the identification of balanced geometrical configurations that deliver improved overall thermal performance rather than favoring a single operating condition.

7.3. TOPSIS-based decision analysis and optimal solution ranking

After generating optimal candidate solutions via multi-objective optimization, the TOPSIS method was used to rank the configurations and identify the most favorable overall design. The TOPSIS procedure begins with normalization of the decision matrix, as expressed in Eq. (17). This equation converts the performance values into dimensionless quantities, ensuring that objective functions with different magnitudes can be compared consistently. The normalization process prevents parameters with larger numerical values from dominating decision-making [61].

$$r_{ij} = \frac{x_{ij}}{\sqrt{\sum_{i=1}^{m} x_{ij}^2}} \tag{17}$$

After normalization, weighting factors are incorporated using Eq. (18) to obtain the weighted normalized matrix [62].

$$v_{ij} = w_j \cdot r_{ij} \tag{18}$$

Eq. (19) specifies the ideal point, defined by selecting the most favorable value of each criterion across all available alternatives. In maximization-type optimization problems, the ideal point is the highest attainable weighted performance for each objective [63].

$$x_j^{ideal} = \max\{v_{ij}\} \tag{19}$$

In contrast, Eq. (20) defines the anti-ideal point as the worst-performing values among the available alternatives [64].

$$x_j^{anti-ideal} = \min\{v_{ij}\} \tag{20}$$

Once the ideal and anti-ideal points are identified, the distances between each candidate solution and the mentioned points are computed using Eqs. (21) and (22) [65].

$$D_i^{ideal} = \sqrt{\sum_{j=1}^{m} w_j\left(x_{ij} - x_j^{ideal}\right)^2} \tag{21}$$

$$D_i^{anti-ideal} = \sqrt{\sum_{j=1}^{m} w_j\left(x_{ij} - x_j^{anti-ideal}\right)^2} \tag{22}$$

Eq. (23) defines the closeness coefficient (CC), which represents each design's relative proximity to the ideal solution. A larger closeness coefficient indicates a more favorable configuration because it minimizes the distance from the ideal solution and maximizes the distance from the anti-ideal solution [66].

$$CC = \frac{D_i^{ideal}}{D_i^{ideal} + D_i^{anti-ideal}} \tag{23}$$

8. Results and discussion

8.1. Thermal performance analysis of the full factorial designs

Table 5 summarizes the thermal performance results from the 27 full-factorial design configurations. The table presents the geometrical variables of each design, including L, D, and α, along with the corresponding absorbed energy values at three charging durations. The selected charging times are 1 h (3600 s), 2 h (7200 s), and 5 h (18,000 s). Selecting multiple charging durations is particularly important in LHSSs because the PCM's thermal behavior changes significantly throughout melting. During the early stages, heat transfer is primarily dominated by conduction near the HTF tubes and fin surfaces. As melting progresses, buoyancy-driven natural convection gradually becomes stronger in the liquid RT50 region, altering the heat transfer mechanism and accelerating thermal transport. In the final stages of melting, the remaining solid PCM regions become increasingly limited and localized, leading to another shift in thermal behavior. Therefore, evaluating absorbed energy at different time intervals provides a more comprehensive understanding of the proposed system's charging characteristics. In addition, the total simulation duration was fixed at 5 h to represent realistic solar thermal operating conditions, where effective sunlight availability is typically limited to 6 h per day. Consequently, the system's thermal response within this operating window becomes highly important for practical energy storage applications.

Table 5 additionally presents the outcomes for the reference core configuration, where only HTF tubes are incorporated into the storage medium and no perforated fin structure is utilized. This reference configuration enables a direct evaluation of the thermal enhancement achieved by the interconnected perforated fin structure introduced in the present work. All fin-network-assisted configurations show a clear improvement in thermal energy absorption compared to the core design.

Table 5
Thermal performance of the 27 full factorial designs in terms of absorbed energy at different charging durations, together with the reference core design without a perforated fin network.

Design number	Factors			Energy absorption (kJ)		
	L (mm)	*D* (mm)	*α* (degree)	3600 s (1 h)	7200 s (2 h)	18,000 s (5 h)
1	15	30	120	5457	7510	9471
2	15	10	120	5268	7501	9996
3	15	30	60	5087	6978	9520
4	15	20	90	5216	7258	9838
5	15	30	90	5155	7151	9532
6	15	10	90	5267	7501	9996
7	15	20	120	5230	7265	9839
8	15	20	60	5124	7087	9814
9	15	10	60	5119	7128	9972
10	10	20	90	5409	7427	9815
11	10	20	60	5338	7246	9803
12	10	30	60	5268	7111	9499
13	10	10	90	5382	7463	9996
14	10	10	120	5419	7636	9979
15	10	10	60	5309	7291	9975
16	10	20	120	5464	7629	9803
17	10	30	90	5383	7324	9505
18	10	30	120	5429	7514	9498
19	5	10	60	5513	7679	9975
20	5	30	120	5562	7620	9473
21	5	30	60	5491	7526	9480
22	5	10	90	5514	7610	9970
23	5	10	120	5570	7763	9957
24	5	20	90	5553	7591	9788
25	5	20	120	5616	7738	9779
26	5	30	90	5521	7548	9479
27	5	20	60	5547	7625	9791
Core-design	–	–	–	1813	3077	5395

During the early charging stage at 1 h, Design 25 exhibits the highest absorbed energy (5616 kJ). In contrast, the core design absorbs only 1813 kJ during the same period. This indicates that Design 25 enhances the short-term energy absorption capability by approximately 209.8% compared with the reference configuration. These results highlight the strong influence of the perforated fin arrangement in enhancing thermal propagation and intensifying the early charging process of RT50, where conductive heat transfer dominates. The superior performance of the perforated fin-assisted configurations during early charging can be explained by the dominant role of conduction heat transfer in the initially solid PCM region. At this stage, the thermal energy transferred from the HTF tubes must propagate through the low-conductivity PCM, resulting in a considerable thermal resistance. The interconnected fin network reduces this resistance by providing highly conductive pathways that transfer heat deeper into the PCM domain. Furthermore, perforations prevent excessive obstruction of PCM movement, allowing the enhanced conductive mechanism to coexist with the development of natural convection as melting progresses. At the 2 h intermediate charging stage, Design 23 achieves the highest thermal energy absorption of 7763 kJ. In comparison, the baseline configuration stores just 3077 kJ of energy, indicating that the modified design achieves nearly 153.2% more energy absorption capacity. The combined influence of conduction via the perforated fin and intensified natural convection in the molten RT50 becomes more pronounced, enabling significantly faster thermal transport throughout the storage domain. At the final charging stage of 5 h, Designs 2, 6, and 13 achieve the maximum absorbed energy value of 9996 kJ among all investigated configurations. Under the same operating conditions, the core design stores only 5395 kJ. Therefore, the optimized fin-assisted configurations provide approximately 85.3% greater absorbed energy than the reference storage unit. Although the percentage enhancement decreases with longer charging durations, the thermal improvement remains highly significant because the PCM approaches complete melting during the later stages of charging.

8.2. *Detailed thermal behavior of selected configurations*

Six representative configurations with distinct geometrical characteristics are selected from the 27 full factorial designs and compared in detail with the reference core design. The selected designs include Designs 1, 9, 10, 19, 21, and 23, which exhibit different thermal responses throughout the charging process. Fig. 5(a) represents the alterations of total absorbed energy over time. A substantial difference is immediately apparent between the fin-network-assisted configurations and the core design without perforated fins. The LHSS containing only HTF tubes exhibits significantly weaker charging behavior throughout the process, confirming that the HTF tubes alone cannot distribute heat effectively within the PCM domain. Even increasing the HTF tube diameter, which naturally enlarges the direct heat transfer surface area, cannot compensate for the absence of the perforated fin network. This clearly demonstrates that the interconnected fin structure plays the dominant role in accelerating thermal transport and distributing energy throughout the storage body.

Among the investigated configurations, Design 23 ($L = 5$ mm, $D = 10$ mm, and $\alpha = 120^{\circ}$) exhibits the fastest total energy absorption during a considerable portion of the charging process. However, this configuration's superiority is mainly observed during the early and intermediate stages of melting, while some configurations with initially lower performance eventually surpass it during the later stages. A representative example is Design 19 ($L = 5$ mm, $D = 10$ mm, and $\alpha = 60^{\circ}$), which has identical perforation length and HTF tube diameter but differs only in the inclination angle. This orientation variation significantly modifies the buoyancy-driven flow pattern inside the molten PCM region and, consequently, affects the interaction between natural convection and heat transfer through the perforated fin network. In Design 23, the 120° inclination angle promotes upward movement of the molten PCM due to the thermosiphon effect generated by density differences between the hotter liquid PCM near the HTF tubes and the colder regions away from the heat source. As the heated PCM rises, it reaches the upper regions of the storage domain where the frontal sections of the fin network provide relatively restricted flow passages. Therefore, the upward movement of the molten PCM is partially hindered, forcing the fluid to redistribute through the available perforation openings. Although this restriction limits the large-scale circulation of liquid PCM, it increases the residence time of the high-temperature molten PCM within the central regions surrounding the heat transfer structures. Consequently, thermal energy remains concentrated near regions with stronger conductive pathways for longer, allowing more effective interaction between the hot PCM, fin surfaces, and surrounding solid PCM. This combined effect enhances heat penetration into the adjacent PCM layers and results in a higher energy absorption rate during the intermediate stages of melting.

In contrast, Design 19 with an inclination angle of 60° provides a more open pathway for upward buoyancy-driven flow. The molten PCM generated near the HTF tubes can move more freely toward the upper regions of the storage domain, resulting in stronger and more extensive natural convection circulation. However, during the early and intermediate stages, this rapid upward transport also decreases the residence time of the high-temperature liquid PCM in the central regions. As a result, although circulation intensity is higher, some thermal energy is transported away from the most effective heat-transfer regions before it is fully distributed throughout the PCM domain. Therefore, Design 19 exhibits a slightly lower energy absorption rate compared with Design 23 during these stages. This behavior indicates that a configuration's effectiveness is mainly determined by its ability to maintain strong thermal interaction between the heated PCM region and the conductive fin network. Since only a limited portion of PCM has melted during this period, the contribution of large-scale natural convection remains relatively limited. Therefore, configurations that enhance heat conduction

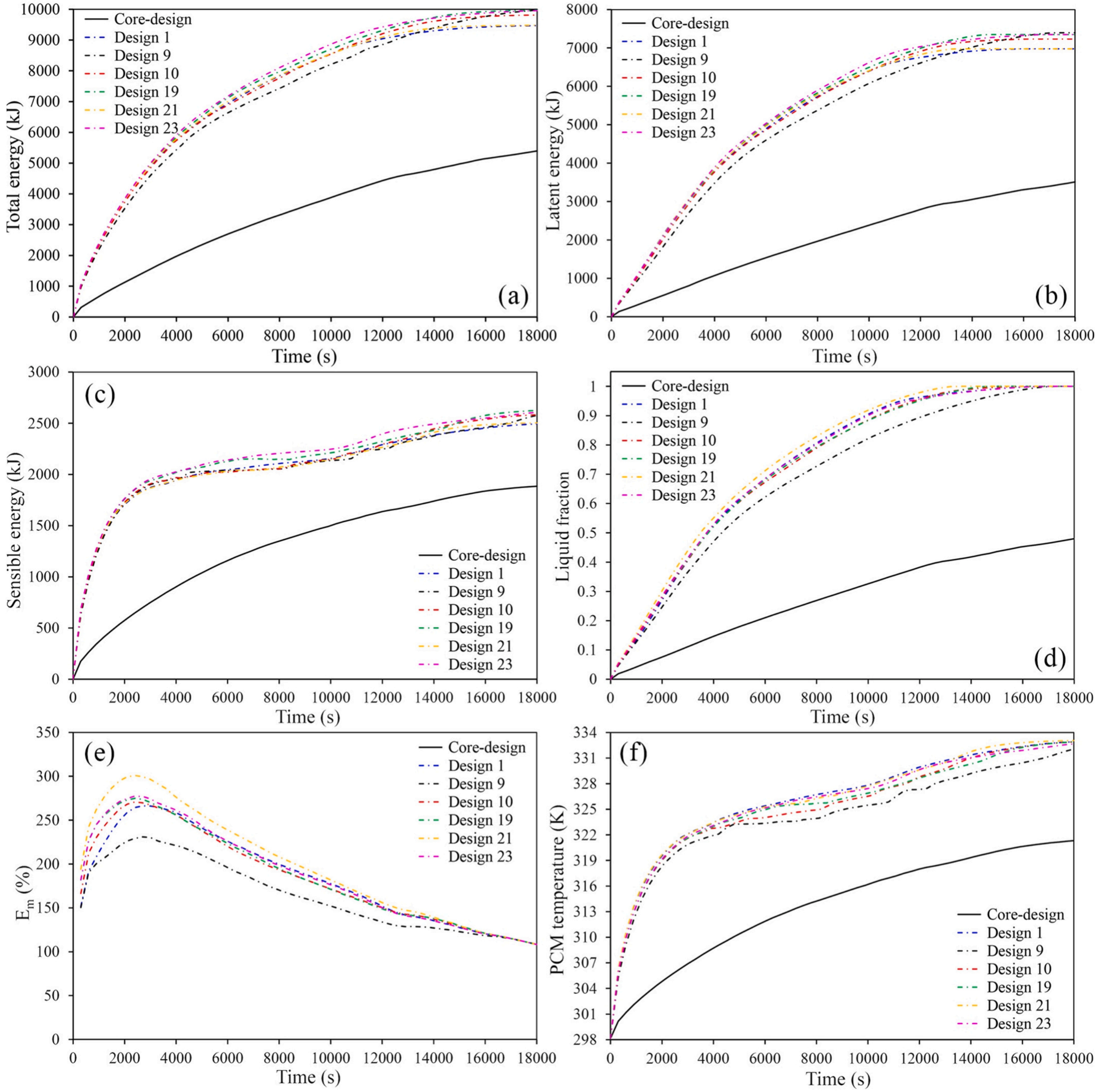

Fig. 5. The thermal characteristics of the selected perforated-fin-assisted designs and the reference core design.

and increase the residence time of hot molten PCM near the heat transfer structures can achieve higher energy absorption rates. As charging continues, the storage system's thermal behavior gradually changes. The PCM temperature approaches the HTF temperature, reducing the temperature difference between the heat source and the PCM and consequently weakening the conductive heat-transfer contribution. Under these conditions, maintaining high-temperature PCM near the central region becomes less dominant, and the ability to establish a broader natural convection circulation becomes increasingly important. Due to its more open flow pathway, Design 19 benefits from enhanced buoyancy-driven circulation during the later stages of melting, allowing thermal energy to be transported more uniformly into previously less-affected PCM regions. Therefore, Design 19 gradually improves its relative performance and eventually surpasses Design 23 in terms of total energy absorption during the final charging stage. The observed performance reversal is associated with the transition of the dominant heat transfer mechanism from conduction-controlled melting to convection-enhanced thermal transport. When a large liquid PCM region develops, buoyancy-driven circulation becomes increasingly important because it determines the system's ability to distribute thermal energy to regions farther from the HTF tubes and fin surfaces. Consequently, geometries that provide less restricted flow pathways can achieve more effective thermal redistribution during the later stages of charging. This transition demonstrates that the optimal configuration in PCM thermal storage systems depends strongly on the dominant heat transfer mechanism at different stages of melting. While Design 23 benefits from controlled PCM circulation and enhanced thermal interaction during the conduction-dominated stages, Design 19 provides superior convective redistribution when natural convection becomes the primary heat transfer mechanism.

Fig. 5(b) demonstrates the latent absorbed energy. Once again, Design 23 initially demonstrates stronger latent heat absorption than Design 19. Since both designs have identical PCM volumes and nearly identical geometries, their maximum latent energy storage capacities are theoretically identical. However, the difference lies in the rate at which latent energy is absorbed. In Design 23, the trapped circulation of high-temperature molten PCM within the central regions enables more effective thermal distribution across the storage body. Instead of rapidly escaping upward, the liquid PCM continuously rotates and transfers energy within the interior regions before gradually moving through the perforations. This behavior promotes more uniform melting and allows the PCM to absorb latent energy more rapidly during intermediate stages. In Design 19, the molten PCM quickly gains energy from the HTF tubes and rises because the flow path is less obstructed. Although this enhances fluid mobility, it reduces the ability of thermal energy to penetrate less accessible PCM regions. Therefore, some areas within the storage body receive heat less effectively during intermediate stages. Nevertheless, the more open circulation path in Design 19 improves overall temperature uniformity within the PCM domain, thereby helping the design exceed Design 23 during later stages of melting.

Fig. 5(c) presents variations in the sensible absorbed energy. Compared with latent energy, differences between the selected configurations are smaller because sensible heat storage mainly depends on the temperature rise before and after the phase-transition intervals. However, all perforated-fin-assisted designs still absorb considerably more sensible energy than the core design, confirming the fin network's strong enhancement of overall thermal transport. Fig. 5 (d) shows the evolution of the liquid fraction. Among all investigated configurations, Design 21 ($L = 5$ mm, $D = 30$ mm, and $\alpha = 60^{\circ}$) achieves the highest liquid fraction throughout the charging process. Compared with Design 19, the main difference between these two configurations is the larger HTF tube diameter in Design 21. Increasing the tube diameter directly increases the contact surface area between the HTF tubes and the surrounding PCM, thereby enhancing the thermal interaction at the solid–liquid interface. Consequently, thermal energy penetrates more rapidly into the surrounding PCM, accelerating the phase transition process and resulting in a faster enhance in liquid fraction. In addition to the enhanced heat-transfer area, the larger HTF tubes change the geometrical distribution of the PCM within the storage domain. Because the HTF tubes occupy a larger portion of the storage volume, less PCM surrounds the tubes. Therefore, the remaining PCM experiences a higher effective heat input per unit mass, allowing a greater fraction of the available PCM to reach the melting temperature within a shorter period. This combination of increased conductive heat transfer and reduced PCM mass explains the superior melting response and higher liquid fraction observed for Design 21 compared with configurations containing smaller HTF tubes. This result demonstrates that melting rate and energy storage capacity represent two different performance aspects in PCM-based systems. Increasing the HTF tube diameter increases the available heat-transfer surface and accelerates phase transition; however, it simultaneously reduces the volume of PCM available for latent heat storage. Therefore, a configuration that achieves faster melting does not necessarily provide the highest thermal energy storage capability. However, the higher liquid fraction achieved by Design 21 should not be interpreted as a direct indication of higher total energy storage capability. The total latent energy stored in a PCM-based system is strongly dependent on both the latent heat of the material and the total mass of PCM undergoing phase transition. Although Design 21 melts a larger fraction of its PCM more rapidly, the available PCM mass is lower because of the increased HTF tube volume. As a result, the total amount of latent heat that can be stored is reduced compared with configurations containing a larger PCM volume. Therefore, Design 21 demonstrates superior melting kinetics and faster phase transition, while configurations with a greater PCM volume may provide higher overall energy storage capacity. This finding highlights the importance of distinguishing between melting-rate indicators, such as liquid fraction, and storage-capacity indicators when evaluating the thermal characteristics of PCM-based LHSSs.

Fig. 5(e) illustrates the melting enhancement ratio (E_m), used to evaluate the melting performance increment of the perforated-fin-assisted designs relative to the core design without fins. The enhancement values are remarkably high during the early charging stages, highlighting the fin network's strong influence on accelerating melting. Design 21 exhibits the maximum enhancement ratio, reaching approximately 301% at nearly 3000 s. This means that the melting performance of Design 21 is more than 3 times that of the core design at this stage. As charging progresses, the enhancement ratios gradually decrease because the core continues to melt, and the relative performance gap narrows. Fig. 5(f) illustrates the average PCM temperature evolution. In the later phase of the melting, Design 21 exhibits the highest PCM temperature among all investigated configurations. This behavior is directly linked to its reduced PCM volume and increased HTF surface area. Since a smaller quantity of PCM absorbs the supplied thermal energy, the average temperature rises more rapidly. Simultaneously, the larger HTF tubes intensify conductive heat transfer and accelerate energy delivery throughout the storage domain. Although Design 21 achieves higher temperatures and faster melting, its sensible energy storage capacity remains lower because the total PCM mass available for energy storage is reduced.

Fig. 6 presents radar-plot comparisons of the total absorbed energy for six representative perforated-fin-assisted configurations discussed in Fig. 5. These plots provide a clearer visualization of how the relative thermal performance of the selected designs changes across different stages of the charging process. Rather than showing the full transient curves, the radar plots focus on three specific operating times: early-stage charging (1 h), intermediate charging (2 h), and long-term charging (5 h). Such a representation allows the evolution of the dominant thermal mechanisms to be interpreted more effectively. Fig. 6 (a) illustrates the absorbed energy after 1 h of charging. At this early stage, Design 23 exhibits the highest energy absorption capability among all investigated configurations, followed closely by Design 19. In contrast, Design 9 ($L = 15$ mm, $D = 10$ mm, and $\alpha = 60^{\circ}$) demonstrates the lowest energy absorption during this period. The overall pattern observed in Fig. 6(a) arises from the fin network's ability to accelerate conductive heat transfer during the initial melting stages.

A very similar behavior is observed in Fig. 6(b), which corresponds to the absorbed energy after 2 h of charging. Once again, Design 23 maintains the highest energy absorption, while Design 19 remains the second-best configuration. Design 9 still exhibits the weakest thermal response among the selected cases. The similarity between the 1 h and 2 h radar patterns suggests that the thermal mechanisms governing the early and intermediate stages of melting remain relatively unchanged. During these periods, the perforated fin network's effectiveness in distributing heat and controlling natural convection plays the dominant role in determining thermal performance. However, Fig. 6(c) shows distinctly different behavior, representing the absorbed energy after 5 h of charging. At this stage, the relative ranking of the designs changes noticeably. Design 19 surpasses Design 23 and becomes the best-performing configuration in terms of total absorbed energy. More importantly, Design 9, which previously performed the weakest in the earlier stages, now shows significantly improved long-term energy absorption and approaches the performance of Designs 19 and 23. Conversely, Design 21 shows reduced relative performance during the later charging stages.

This transition in thermal behavior can be explained by examining how the geometrical parameters influence the total PCM volume within the storage body. Design 9's higher energy-absorption capacity than Design 19 is mainly due to its longer perforation length (L). Since the other geometric parameters are identical, the difference in thermal behavior originates from the fluid flow path created by the larger

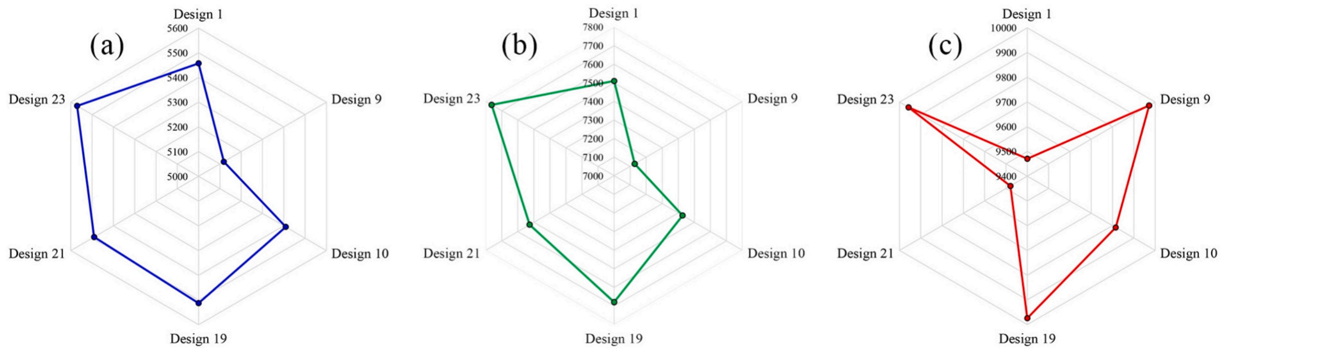

Fig. 6. Radar-plot comparison of total absorbed energy for selected perforated-fin-assisted configurations at different charging durations: (a) 1 h, (b) 2 h, and (c) 5 h.

perforations. In Design 9, the molten PCM can move upward more easily due to reduced flow resistance, thereby strengthening the natural convection currents within the storage body. As a result, thermal energy is transported more rapidly toward the upper regions of the system. Although this initially reduces the heat transfer intensity in the lower and side regions adjacent to the storage body, the continuous circulation of the molten PCM gradually redistributes the absorbed thermal energy throughout the domain. Therefore, over long operating times, Design 9 benefits from improved overall energy distribution and ultimately achieves higher total energy absorption than Design 19. In the long term, as the system approaches its maximum liquid fraction and the PCM temperature approaches the HTF temperature, the total PCM mass becomes increasingly important. Under these conditions, a larger PCM volume enables the system to absorb and store more thermal energy, which explains the improved long-term performance of Design 9. Design 21 shows the opposite thermal behavior. In this configuration, the HTF tube diameter D is the largest among the selected designs. Enlarging the HTF tubes increases the heat transfer surface area and accelerates melting during the early stages, which explains the strong short-term thermal response of this design. However, larger HTF tubes occupy a larger portion of the storage domain, thereby reducing the available PCM volume. As the charging process progresses toward completion, the lower PCM quantity reduces the system's overall thermal energy storage capability. Therefore, although Design 21 exhibits rapid melting and high liquid fractions, its long-term energy absorption is weaker than that of configurations with larger PCM volumes.

To further evaluate the validity of the assumption regarding negligible axial temperature variation, an additional analysis was performed based on the energy balance of the HTF. According to the numerical results for all 27 design configurations, the total energy absorbed by the PCM after 5 h of charging is approximately 9400–10,000 kJ. Considering the energy balance equation: $\dot{Q} = \dot{m}C_p\Delta T$, the required HTF mass flow rate was estimated. In this calculation, the HTF thermophysical properties were evaluated at the operating temperature of 333.15 K, and the axial temperature variation was assumed to be approximately 0.5 K. Based on the absorbed energy range from the simulations, the required total mass flow rate and corresponding volumetric flow rate were calculated. The results indicate that the required volumetric flow rate for the entire storage system is approximately 15–16.2 L/min. Since the proposed system contains eight HTF tubes, the corresponding flow rate per tube is estimated to be approximately 1.875–2.025 L/min. This range represents a realistic operating condition for similar thermal storage systems and confirms that the HTF flow rate is sufficiently high to maintain a very small axial temperature variation. This estimation provides a general assessment of the required flow rate range for the investigated system rather than a separate flow analysis for each of the 27 configurations. Although variations in tube diameter and inclination angle can influence the PCM's thermal response, their effects are mainly associated with PCM-side heat transfer mechanisms, while the axial temperature variation of the HTF remains relatively limited due to continuous fluid circulation. Therefore, the 2D approximation remains valid for the investigated parametric range. Furthermore, a limitation of this estimation is that part of the supplied thermal energy is also absorbed by the copper fin network and solid components. Because this amount is considerably smaller than the total energy stored by the PCM, it was neglected in the present calculation. Including the energy absorbed by the solid structures would slightly increase the estimated required HTF flow rate; however, it would not significantly alter the conclusion regarding the validity of the 2D modeling assumption.

8.3. Accuracy and predictive capability of the developed MLP model

Before employing the MLP model for prediction, it was necessary to determine the most suitable network architecture, as schematically illustrated in Fig. 4(a). Selecting a neural network structure is one of the most important stages in machine learning applications because a weak network cannot accurately capture physical behavior. In contrast, an overly complex network may memorize the training data and lose its generalization capability. Therefore, a systematic trial-and-error procedure was performed to determine the optimal architecture. The network complexity was gradually increased in steps. To determine the optimal network architecture, a systematic sensitivity analysis was performed. Initially, the number of hidden layers was gradually increased to evaluate its influence on prediction accuracy. The findings indicated that adding more than a single hidden layer provided no significant enhancement in the model's prediction accuracy, while increasing computational complexity and reducing model efficiency. Subsequently, the number of neurons in the hidden layer was varied to identify the optimal network size. Increasing the number of neurons improved prediction accuracy up to 10 neurons; however, further increases resulted in excellent performance on the training data but diminished accuracy on unseen datasets. This behavior indicates overfitting, where the network learns the training samples too well and loses generalization capability. The previously obtained thermal responses from the 27 full-factorial simulations were used here as benchmark data for training, validation, and testing of the network. Accordingly, the final MLP architecture was selected as a 3–10–2 structure, consisting of three neurons in the input layer corresponding to L, D, and α, one hidden layer containing 10 neurons, and two neurons in the output layer representing STE and LTE. Tangent sigmoid activation functions (tansig) were employed in the hidden layer to capture nonlinear relationships between the input parameters and thermal responses. In contrast, a linear activation function (purelin) was used in the output layer to provide continuous numerical predictions. This optimized architecture balances prediction accuracy, computational efficiency, and generalization capability.

Detailed information regarding the developed network is presented in Table 6. The table lists the weights and biases for both the hidden and output layers of the final MLP model. These parameters represent the mathematical relationships the neural network learned during training.

Table 6
Detailed information on the developed MLP prediction model for STE and LTE responses.

Hidden layer				Output layer			
Weights (10 × 3)			Biases (10 × 1)	Weights^T (10 × 1)		Bias (1 × 1)	
				STE	*LTE*	*STE*	*LTE*
1.443	1.918	0.476	−3.915	1.189	−0.307	1.412	−0.670
2.100	1.837	0.466	−2.329	−0.551	0.084		
1.858	−2.954	1.257	−2.362	0.044	−0.008		
−0.027	0.701	0.015	−0.448	−0.364	−1.569		
2.122	−0.841	2.456	0.835	−0.214	0.078		
1.886	2.341	−1.965	−0.303	0.039	−0.085		
1.918	0.254	−2.680	−1.318	0.033	0.011		
−1.008	0.604	2.816	−2.448	0.445	−0.080		
−0.802	−0.486	−2.958	−1.941	−0.707	0.018		
2.228	0.429	2.405	3.238	−0.786	−0.013		

The hidden-layer weights determine how strongly each geometric parameter influences the neurons, while the output-layer weights determine how the hidden neurons contribute to predicting *STE* and *LTE*. Therefore, Table 6 provides the complete mathematical foundation of the developed prediction model and enables future researchers to reproduce the trained network directly without retraining.

Table 7 evaluates the predictive accuracy of the developed MLP model using two key statistical performance indices: RMSE and R^2. RMSE indicates the model's average prediction error, while R2 measures how well the network captures the relationship between inputs and outputs. Lower RMSE values and R^2 values approaching unity indicate higher prediction accuracy. According to Table 7, the developed MLP model achieved RMSE values of 21.201 and 8.393 for *STE* and *LTE*, respectively. In addition, the obtained R^2 values were 0.990 for *STE* and 0.998 for *LTE*. The extremely high R^2 values indicate that the model successfully captured the nonlinear thermal behavior of the PCM storage system with very high precision. Furthermore, the relatively low RMSE values confirm that the deviations between the predicted and simulated data are minimal. Therefore, the developed MLP model can be considered a highly reliable and efficient predictive tool for estimating the thermal performance of the proposed LHSS.

In machine learning applications, developing a prediction model alone is not sufficient. The model must also demonstrate that it can accurately reproduce the physical behavior obtained from numerical simulations. Therefore, the results presented in Fig. 7 are extremely important because they visually demonstrate the agreement between the numerical data and the neural network's predictions. Fig. 7(a) and (b) compare the numerical simulation results with the predictions of the developed MLP model for *STE* and *LTE*, respectively. In these plots, the solid diagonal line represents the ideal case where the predicted values exactly match the numerical results. Therefore, the closer the data points are to this diagonal line, the more accurate the prediction model becomes. In Fig. 7(a), nearly all data points lie directly on or very close to the diagonal line, and the predicted *STE* values show an excellent agreement with the numerical data.

A similar trend can be observed in Fig. 7(b) for *LTE* prediction. In fact, the agreement between the numerical and predicted *LTE* results is even stronger. The predicted values almost perfectly overlap the numerical data, demonstrating the outstanding predictive capability of the developed network for the long-term thermal performance of the PCM storage system. Fig. 7(c) and (d) further investigate the model's predictive accuracy by presenting the relative prediction errors for *STE* and *LTE* across all 27 designs. These plots are especially useful because they allow the error distribution across different geometrical configurations to be examined individually, rather than relying solely on global statistical indicators such as RMSE and R^2. In Fig. 7(c), the relative errors for STE remain remarkably small across all designs. Most prediction errors are significantly below 1%, indicating that the developed neural network provides highly reliable short-term predictions. The maximum relative error is observed for Design 20 at approximately 0.991%, which is still extremely small from an engineering perspective. These low deviations indicate that the MLP model generalizes well and does not merely memorize the training dataset.

Table 7
Performance indices of the developed MLP model for predicting STE and LTE responses.

Cost function	MLP prediction model	
	STE	*LTE*
RMSE	21.201	8.393
R^2	0.990	0.998

Similarly, Fig. 7(d) demonstrates the relative prediction errors for *LTE*. The errors are even smaller than those for *STE* predictions. Most LTE prediction errors remain below 0.2%, with the maximum observed error of approximately 0.303% for Design 11. These very small deviations confirm that the developed MLP model can predict long-term thermal behavior with exceptionally high precision. From a thermal engineering and machine learning perspective, these results are highly important. Numerical simulations of PCM systems are often computationally intensive due to the strong coupling among conduction, convection, and phase change processes. However, once a reliable neural network model is trained, it can predict the thermal performance of new geometrical configurations almost instantly. Therefore, the developed MLP model not only demonstrates high predictive accuracy but also provides a highly efficient alternative tool for future optimization and design studies of LHSSs.

Sufficient training data is critical to developing reliable machine learning models. However, in the present study, generating a large dataset through numerical simulations is computationally expensive because each transient PCM melting simulation requires considerable computational time. Therefore, performing hundreds of simulations, as commonly performed in purely data-driven studies, is not practically feasible for the present high-fidelity thermo-fluid model. To address this issue, a full-factorial design of experiments (DoE) approach was adopted. Unlike random sampling methods, the full-factorial design systematically investigates all possible combinations of the selected design variables within the defined levels (27 datasets). These variables were not selected arbitrarily; rather, they were identified as the most influential geometrical factors affecting the thermal response of the proposed LHSS. Furthermore, the selected ranges were determined based on their physical influence and geometrical limitations, ensuring that the generated dataset adequately represents the investigated design space. The MLP model was not trained using all 27 datasets. A portion of the available data was reserved as unseen data for independent evaluation. Specifically, 70% of the datasets were randomly assigned for training, while the remaining 30% were excluded from training and used only to evaluate the predictive capability of the developed model. Therefore, the results presented in Table 7 and Fig. 7 correspond to the complete dataset, including both training and unseen samples, rather than only

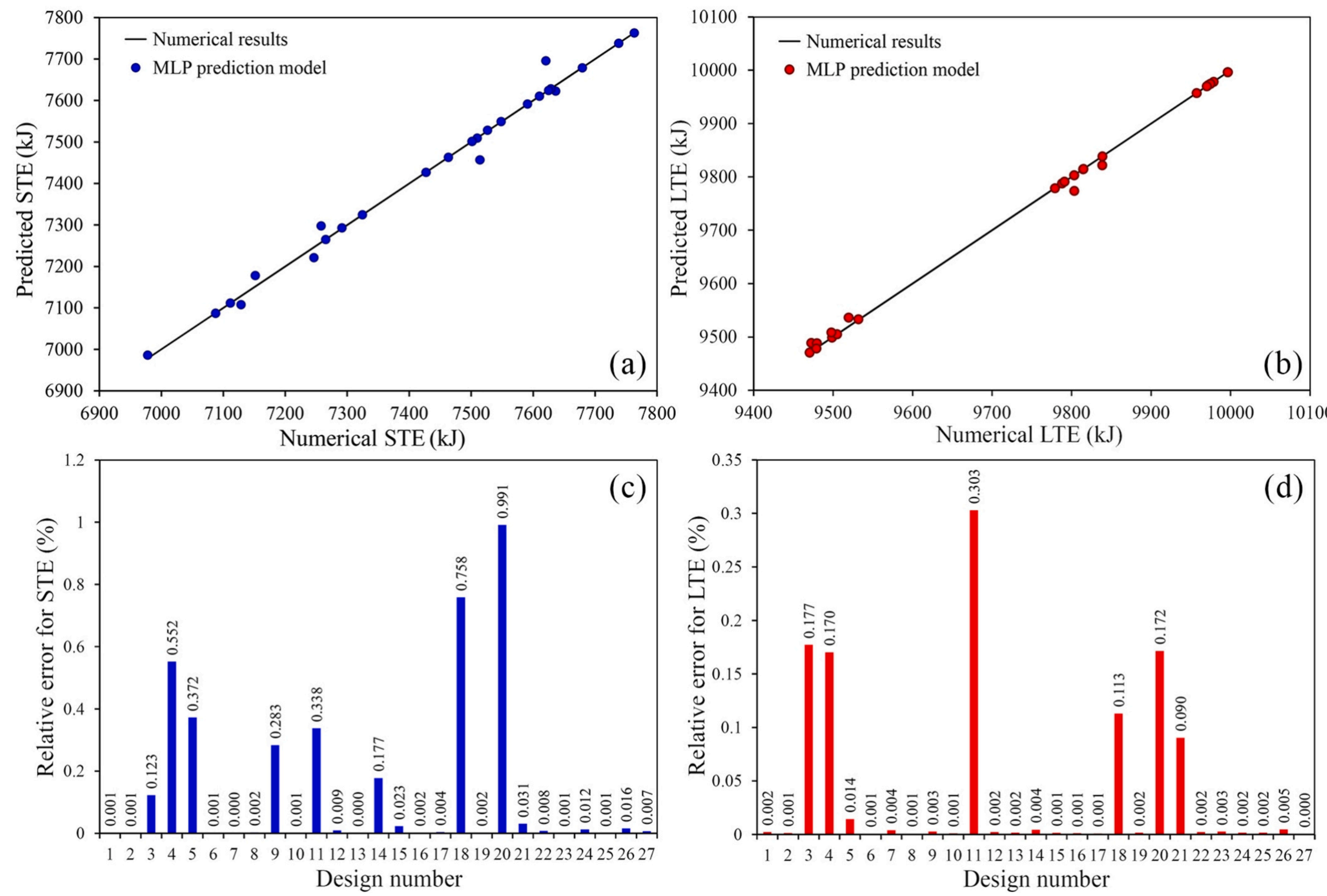

Fig. 7. Comparison of numerical and predicted (a) STE values, (b) LTE values. Relative prediction error of the MLP model for (c) STE and (d) LTE.

the data used for model training. The very low prediction errors and the high R^2 values demonstrate that the developed MLP model can accurately predict both seen and unseen data. This confirms that the model does not simply memorize the training samples and that overfitting did not occur. Furthermore, to provide additional evidence of the model's generalization capability, K-fold cross-validation was performed. This approach is particularly suitable for limited datasets because it evaluates the model's robustness across different data partitions. The outcomes of the K-fold demonstrated that the R^2 value consistently remained above 98% across all folds. This confirms the stability of the developed MLP model and indicates that the prediction accuracy is not significantly affected by the selected data partitioning. In addition to data-based validation, we also examined the possibility of overfitting through network architecture optimization. Increasing the number of neurons initially improves the model's predictive capability; however, after reaching an optimum number of neurons, further increases improve training accuracy while gradually reducing accuracy on unseen data. This behavior clearly indicates overfitting. Therefore, the final network architecture was selected based on the best balance between training accuracy and generalization capability, avoiding unnecessary model complexity. Finally, the developed MLP model is intended specifically for the proposed latent heat storage configuration and the investigated ranges of geometrical parameters. The model is not claimed to predict completely different storage geometries or operating conditions outside the defined design space. However, since the selected parameters represent the dominant geometrical factors governing the thermal response, and the underlying heat transfer mechanisms remain unchanged, the developed model is expected to provide reliable predictions for geometrically similar systems, including scaled versions of the proposed configuration.

8.4. Sensitivity analysis of geometrical parameters on thermal performance

Fig. 8 presents the sensitivity analysis results derived from the developed MLP model. These 3D response surfaces are extremely valuable because they help visualize how the geometric parameters interact. Fig. 8(a) – (c) illustrate the variation of *STE* with respect to the geometrical parameters. One important observation is that *STE*'s behavior is more complex than *LTE*'s. This complexity arises from the transient nature of the early melting stages, where conduction and natural convection interact and depend strongly on the flow structure within the molten PCM region. Fig. 8(a) demonstrates the combined effects of L and D on *STE*. Increasing D decreases *STE*. This trend becomes especially noticeable at larger L values. Physically, increasing the tube diameter reduces the available PCM volume within the storage body. Although larger tubes provide greater heat-transfer surface area, the reduction in PCM quantity becomes dominant during short-term operation, resulting in lower absorbed energy. In addition, increasing L also decreases *STE*, particularly at larger D values. Larger perforations facilitate molten PCM flow and reduce the fin surface available for heat transfer into the PCM region, thereby weakening short-term thermal storage capability.

Fig. 8(b) presents the interaction between L and α on *STE*. Increasing L generally decreases *STE*. However, the effect of α is more complicated. At larger L values, increasing α initially increases *STE* and afterwards its intensity decreases. In contrast, at smaller L values, increasing α first decreases *STE*, then increases, with a gentle slope. This behavior highlights the strong coupling between the flow circulation path and the perforation geometry. Different angular configurations alter the thermosiphon-driven flow of molten PCM, thereby altering the

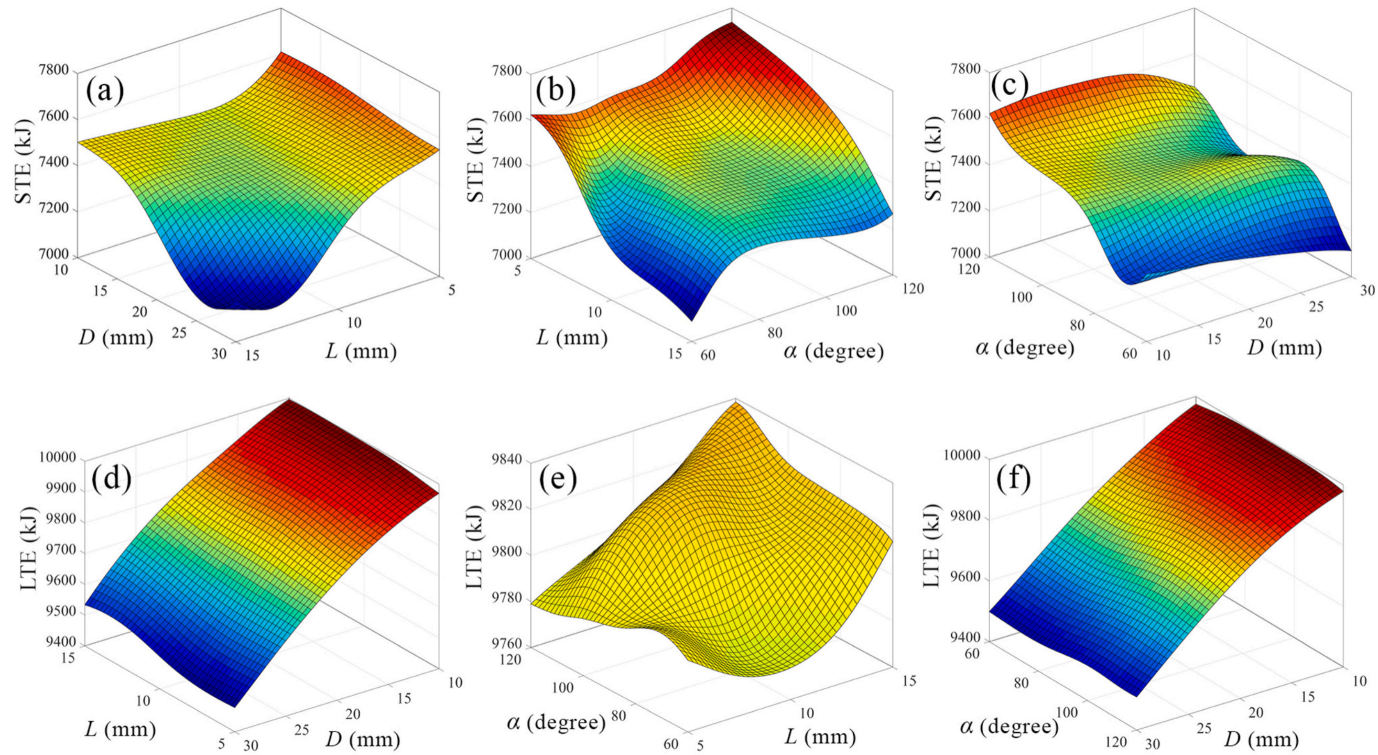

Fig. 8. Sensitivity analysis of short-term and long-term energy absorption responses based on the developed MLP prediction model: (a–c) effects of geometrical parameters on STE and (d–f) effects of geometrical parameters on LTE.

distribution of thermal energy within the storage body. The interaction between α and D is illustrated in Fig. 8(c). Increasing α generally increases *STE*, especially at lower D values. In systems with smaller HTF tubes, the PCM volume is larger, and natural convection has a greater influence. Therefore, modifying the placement angle significantly affects the circulation behavior of the molten PCM and enhances short-term heat absorption. However, at larger D values, the effect of α becomes more nonlinear. Increasing α at different tube diameters increases *STE*, and its effect is nearly the same across all diameters. Meanwhile, increasing D consistently decreases *STE*. Overall, these observations show that *STE* is highly sensitive to the coupled interaction between heat-transfer enhancement and PCM flow structure.

Fig. 8(d) – (f) present the sensitivity analysis for *LTE*. Compared to *STE*, *LTE* behavior is considerably smoother and less complex because the system approaches thermal equilibrium during the later charging phase. In Fig. 8(d), increasing D decreases *LTE* at all values of L. This behavior is expected because larger HTF tubes reduce the total PCM volume, thereby limiting the maximum thermal energy that can be absorbed over the long term. In contrast, increasing L increases *LTE* at all D values. Larger perforations provide larger PCM regions and improve thermal energy storage capacity during extended operation. Fig. 8(e) illustrates the combined effects of L and α on *LTE*. One noticeable observation in this plot is the relatively limited color variation compared to the other figures. This weaker color spectrum indicates that *LTE* is not highly sensitive to the parameters L and α. Instead, *LTE* is considerably more sensitive to parameter D. At the same time, L and α still influence melting behavior; however, their effects on long-term thermal storage are less significant than the influence of HTF tube diameter. Fig. 8(f) presents the interaction between D and α on *LTE*. Increasing D decreases *LTE* for all values of α, again because it reduces PCM volume. A trade-off between heat transfer enhancement and PCM storage capacity therefore governs the influence of HTF tube diameter. Although larger tubes provide a greater contact area for heat exchange, they occupy a larger portion of the storage volume and reduce the amount of PCM available for latent heat absorption. This trade-off becomes particularly important when evaluating the total absorbed energy, where maintaining sufficient PCM mass is essential for achieving high storage capacity. The effect of α on *LTE* is relatively small compared with the other geometrical parameters. However, in general, increasing α slightly improves *LTE* by partially restricting the upward movement of molten PCM within the storage body. This restriction slows the direct escape of high-temperature fluid toward the upper regions and promotes longer thermal interaction within the central sections of the system. As a result, heat is distributed more effectively throughout the PCM domain, leading to a modest enhancement in long-term energy absorption.

8.5. Single-objective optimization analysis using GA

All previous analyses, including the numerical simulations and MLP-based predictions, provide valuable insights into the thermal behavior of the proposed LHSS. However, these data primarily estimate the influence of design parameters on system performance. To identify the truly optimal geometrical configurations for specific performance objectives herein, a systematic GA optimization method is selected. The selection of the GA was based on the characteristics of the optimization problem. The thermal performance of the proposed LHSS is governed by highly nonlinear interactions among the geometrical parameters, heat conduction through the fin network, and buoyancy-driven natural convection within the molten PCM. Therefore, the relationship between the variables and the targets is nonlinear and does not necessarily exhibit a convex behavior. Gradient-based optimization methods such as fmincon are highly effective for smooth, differentiable problems with well-behaved objective-function landscapes. However, they may converge to local optima when applied to complex nonlinear problems with multiple interacting variables and irregular response surfaces. GA, on the other hand, utilizes a population of potential solutions to explore the global search space and does not depend on gradient-based information. It can efficiently explore a wide design space while reducing the likelihood of getting trapped in local optima. Random search was also considered less suitable because, although it can explore the design space without requiring mathematical assumptions, it does not use information from previous evaluations to improve future generations. Consequently, it may require many function evaluations to achieve a satisfactory solution, making it computationally inefficient for optimization problems involving expensive numerical simulations.

Two independent targets are considered in the single-objective optimization: maximizing *STE* and maximizing *LTE*. By applying the GA to each objective separately, two distinct optimal configurations are identified: *OSTE*, optimized for short-term energy absorption, and *OLTE*, optimized for long-term energy absorption. Table 8 summarizes the results of these single-objective optimizations. The geometric parameters for each optimal design, including *L*, *D*, and α, are listed alongside the corresponding numerical simulation results and the predictions obtained from the trained MLP model. The close agreement between the numerical and predicted values confirms the neural network's accuracy and reliability in forecasting system performance across the design space.

When the primary objective is maximizing the total energy-storage capacity, a configuration with a reduced PCM volume should not be considered optimal solely because it exhibits a higher liquid fraction. In the present study, Design 21 is not identified as the optimum configuration for total or long-term energy storage. Rather, it was selected as a representative configuration (among the 27 investigated designs) to illustrate the trade-off between rapid melting and total storage capacity. Design 21 ($L = 5$ mm, $D = 30$ mm, $\alpha = 60^{\circ}$) exhibits the highest liquid fraction because the larger HTF tube diameter increases the direct heat-transfer area and accelerates heat transfer into the surrounding PCM. However, the larger tube diameter simultaneously occupies a greater portion of the storage volume and therefore reduces the amount of PCM available for energy storage. Consequently, although a larger fraction of the available PCM melts rapidly, the absolute amount of PCM that can ultimately store latent energy is reduced. This distinction explains why a high liquid fraction does not necessarily correspond to a high total absorbed energy. This trade-off is particularly important during the transition from short-term to long-term charging. During the early stages, increasing the heat-transfer area can be beneficial because rapid heat penetration and melting are dominant. However, as the system approaches thermal equilibrium, the available PCM mass becomes increasingly important, and the reduction in PCM volume associated with larger tube diameters limits the maximum energy-storage capacity. This behavior is also confirmed by the sensitivity analysis, where increasing the HTF tube diameter consistently decreases long-term energy absorption. Accordingly, practical tube-diameter selection should not be based solely on maximizing liquid fraction. Instead, it should be selected according to the required balance between charging rate and storage capacity. For applications requiring rapid heat absorption over a limited charging period, a larger tube diameter may provide a thermal-response advantage. In contrast, when maximizing the total stored energy over longer operating periods is the priority, a smaller tube diameter is preferable because it preserves a larger PCM volume. This trade-off is reflected in the optimization results of the present study. The GA identified $D = 10$ mm for both *OSTE* and *OLTE* configurations, while the two designs differed mainly in perforation length and inclination angle. Thus, Design 21 should be interpreted as a high-melting-rate configuration rather than an overall optimal design. The final optimization shows that an appropriate tube diameter must balance heat-transfer enhancement with preservation of PCM volume.

8.6. Multi-objective optimization analysis using GA

Fig. 9 presents the distribution of GA-evaluated candidate configurations in the *STE–LTE* performance space. The red markers indicate the Pareto front, representing the set of non-dominated solutions that balance competing objectives. The yellow markers highlight the TOPSIS-selected solutions, demonstrating the designs that best balance short-term and long-term performance. Randomly generated configurations are represented with green markers, providing context for the performance improvements achieved through optimization. The solutions selected by the TOPSIS method are mainly concentrated around the *OSTE* configuration. In fact, TOPSIS selects the *OSTE* scheme as the best solution. By considering both performance objectives together, the multi-objective representation in Fig. 9 provides a more comprehensive understanding of system capabilities. The difference between *OSTE* and *OLTE* in long-term energy absorption is very small (approximately 0.54%), while OSTE demonstrates considerably higher energy absorption during the short- and intermediate-term charging periods. From an engineering perspective, where the available charging period is often limited by the duration of solar radiation or intermittent heat availability, *OSTE* is a more favorable configuration due to its superior transient thermal response. Furthermore, to identify a balanced practical design that considers both performance objectives simultaneously, the final selected configuration was *OSTE*. Therefore, based on both single-objective and multi-objective optimization results, OSTE is selected as the final recommended design in this study because it provides superior short-term performance while maintaining nearly identical long-term energy storage capability compared with *OLTE*. In the original TOPSIS analysis, equal importance was assigned to both objective functions; therefore, the weighting factors for short-term energy absorption (STE) and long-term energy absorption (LTE) were set to

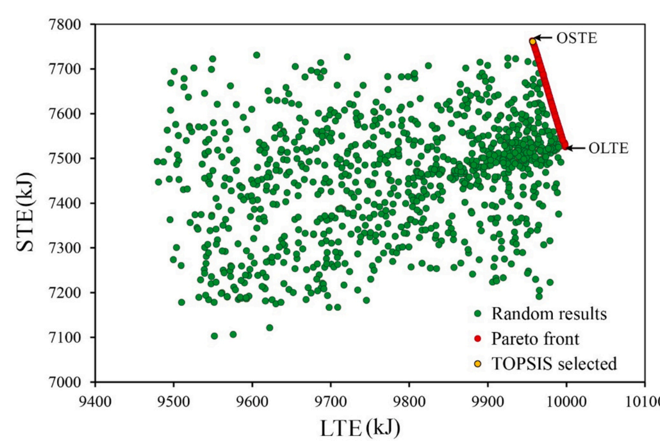

Fig. 9. GA-based optimization results for the proposed LHSS: random candidate configurations (green), Pareto front (red), and TOPSIS-selected solutions (yellow). (For interpretation of the references to color in this figure legend, the reader is referred to the web version of this article.)

Table 8
Optimized LHSS configurations obtained from single-objective GA analysis for OSTE and OLTE, including geometric parameters and comparison between numerical and predicted responses.

Target response	Variables			Results (kJ)				Design label
	L (mm)	*D* (mm)	α (degree)	Numerical		MLP		
				STE	*LTE*	*STE*	*LTE*	
STE	5	10	120	7763	9957	7762	9957	*OSTE*
LTE	15	10	104.220	7343	10,011	7524	9999	*OLTE*

50% and 50%, respectively. Under these weighting conditions, the TOPSIS method selected the *OSTE* configuration as the final optimal solution, with a closeness coefficient of 0.879. An additional sensitivity analysis was then performed to investigate the influence of different weighting factors on the final decision. Two additional weighting scenarios were considered: *STE/LTE* weights of 25%/75% and 75%/25%. The results showed that the selected optimal configuration remained unchanged in all investigated cases, and *OSTE* was identified as the preferred solution regardless of the applied weighting factors. This consistent selection can be attributed to the significant difference between the short-term performance of the optimized configurations and their very similar long-term energy absorption capability. Therefore, *OSTE*'s dominance in transient thermal performance leads to its selection under different TOPSIS weighting conditions.

To better understand the thermal behavior of the optimized designs, Fig. 10 compares the transient thermal responses of the *OSTE* and *OLTE* configurations with those of the reference core design. Fig. 10(a) presents the variation of total absorbed energy with time. Both optimized designs perform substantially better than the core design throughout the entire charging process. The perforated fin network dramatically accelerates heat transfer within the storage body and enhances the PCM's melting performance. Among the optimized cases, the *OSTE*

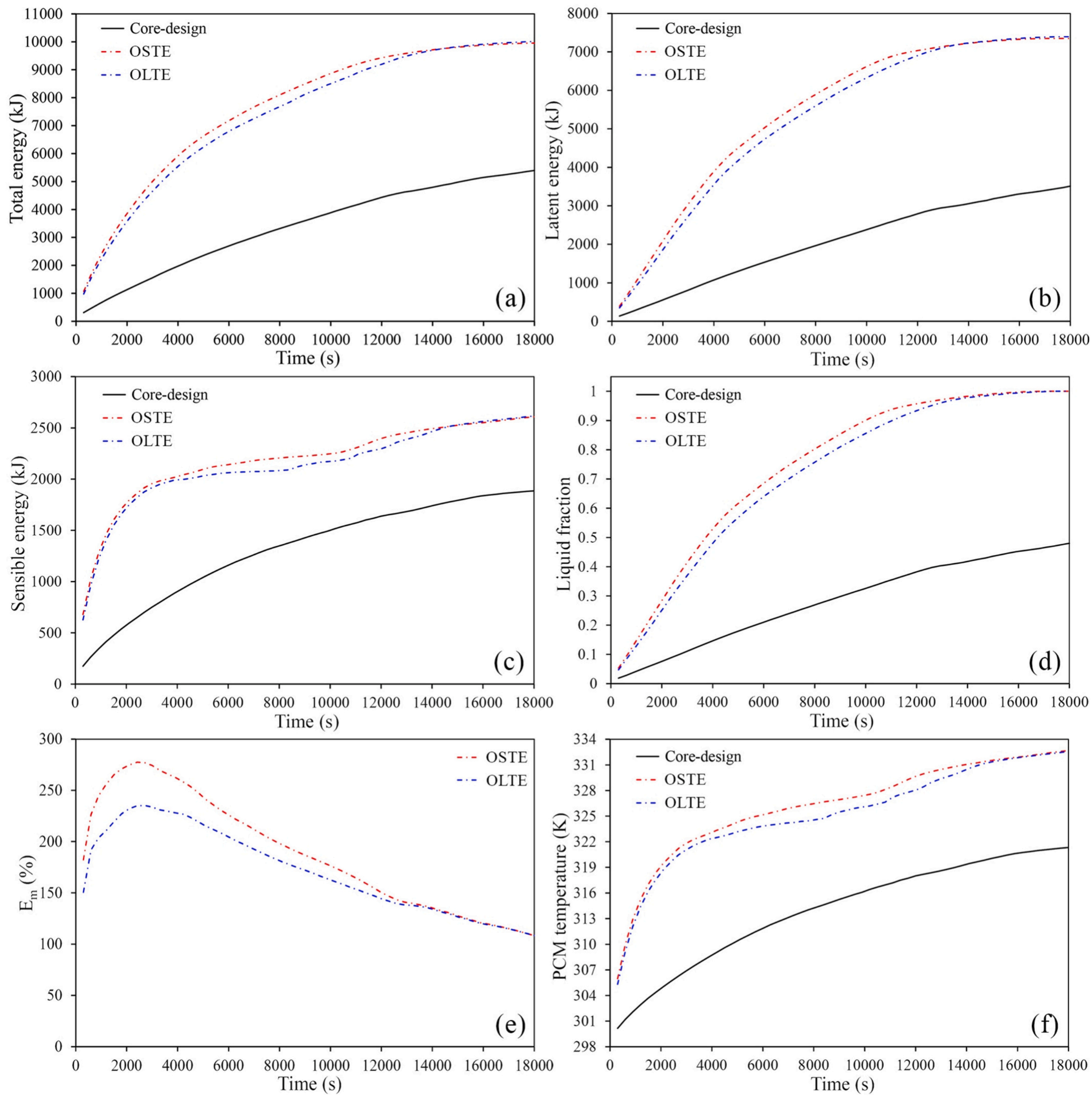

Fig. 10. A comparative assessment of the thermal behavior exhibited by the baseline core configuration, OSTE (optimal short-term energy absorption design), and OLTE (optimal long-term energy absorption design): (a) total energy, (b) latent energy, (c) sensible energy, (d) liquid fraction, (e) melting enhancement ratio (E_m), and (f) average PCM temperature variation over time.

configuration exhibits faster energy absorption during all melting stages. This behavior is expected because the *OSTE* design was specifically optimized to maximize short-term energy absorption. According to Table 8, the *OSTE* design absorbs 7763 kJ under short-term conditions, whereas the *OLTE* design absorbs 7343 kJ. Therefore, *OSTE* achieves approximately 5.72% higher short-term energy absorption than *OLTE*. In comparison, the core design absorbs only 3077 kJ at the same operating time. Therefore, the *OSTE* configuration improves the short-term energy absorption by approximately 152.3% relative to the core design, while the *OLTE* configuration achieves an improvement of about 138.6%. In the final stages of melting, the *OLTE* configuration gradually surpasses *OSTE*. At long-term conditions, *OLTE* absorbs 10,011 kJ, while *OSTE* absorbs 9957 kJ, corresponding to only about 0.54% higher long-term energy absorption for *OLTE*. This comparison clearly indicates that *OSTE*'s superiority throughout most of the charging process is much greater than *OLTE*'s relatively small advantage at the final stage. The difference between the optimized configurations can be attributed to the conflicting physical requirements of short-term and long-term charging. The *OSTE* configuration favors rapid heat penetration by improving the early-stage heat transfer rate, where conduction enhancement plays a dominant role. In contrast, the *OLTE* configuration preserves a larger effective PCM volume, which becomes more beneficial as the system approaches complete melting and total latent heat storage capacity becomes the controlling factor. The core design, however, absorbs only 5395 kJ. Accordingly, the *OLTE* design improves long-term energy absorption by approximately 85.6%, whereas the OSTE configuration improves it by nearly 84.6% compared with the core design.

This behavior is closely related to the geometrical characteristics of the two optimized configurations. In *OSTE*, the smaller perforation length and larger angular configuration promote thermal energy accumulation within the central regions of the storage body. Hence, heat remains concentrated near the HTF tubes for longer, intensifying the melting rate during the medium stages of charging. In contrast, the *OLTE* design allows thermal energy to spread more uniformly toward the upper regions of the PCM domain, resulting in slightly better final energy storage capacity. Fig. 10(b) illustrates the latent energy absorption of the investigated designs. Similar to the total energy behavior, the *OSTE* configuration absorbs latent heat more rapidly during the early and middle stages of charging. This indicates a faster melting process and a stronger phase-change activity. However, toward the end of the process, *OLTE* gradually approaches and slightly exceeds *OSTE*. Since latent energy absorption is directly related to the amount of melted PCM, this result confirms that the *OLTE* design ultimately melts a slightly larger portion of PCM in the final stage of operation.

Fig. 10(c) presents the sensible energy absorption behavior. The differences between *OSTE* and *OLTE* are smaller in this figure compared to the latent energy results. Nevertheless, *OSTE* still shows slightly higher sensible energy absorption throughout most of the charging process due to its faster temperature rise in the system's central regions. As time elapses and the RT50 temperature approaches that of the HTF, sensible heating weakens, and the behavior of the two optimized designs gradually converges. Fig. 10 (d) shows the variations in the liquid fraction. The *OSTE* design achieves higher liquid fraction values throughout most of the charging period, indicating faster melting kinetics. This behavior again confirms the effectiveness of the *OSTE* geometry in accelerating heat penetration into the PCM domain. However, in the final phase of the process, the *OLTE* design catches up, and both configurations eventually approach complete melting conditions. Compared with the core design, both optimized configurations exhibit significantly higher melting rates and shorter charging durations.

The melting enhancement (E_m) is remarkably high during the early stages of charging. The *OSTE* design reaches an E_m value of 277.4% at approximately 2400 s, while the *OLTE* design reaches 235% at the same instant. These values clearly demonstrate the strong contribution of the perforated fin network to accelerating thermal energy transport inside the PCM. The greater *OSTE* enhancement can be attributed to its larger α value and smaller L value. This configuration restricts the rapid upward movement of the molten PCM, keeping thermal energy concentrated in the central sections of the storage body, thereby intensifying local melting and increasing heat-transfer effectiveness. In contrast, the *OLTE* configuration possesses a larger L value, resulting in a larger PCM volume. Consequently, although its melting enhancement is slightly lower during the initial stages, the total energy that can eventually be absorbed increases.

The apparent difference between the maximum E_m and the complete melting time can be explained by considering the definition and physical meaning of the E_m. In this study, E_m is an instantaneous performance indicator calculated at a specific charging time by comparing the liquid fraction of a fin-assisted configuration with that of the reference core design without fins. For instance, the reported maximum E_m of approximately 301% corresponds only to Design 21 (Fig. 5e) at 2400 s, indicating that at this moment the melting progress of Design 21 was about three times that of the core design. It does not represent a three-fold reduction in the total melting time or a constant enhancement throughout the entire charging process. The liquid fraction evolution represents the overall melting progress over the complete charging period. Based on the results, Design 21 reaches complete melting at approximately 13,282 s, while the optimized OSTE and OLTE configurations reach complete melting at approximately 17,013 s and 17,492 s, respectively. Although Design 21 shows a faster phase-transition rate in the early stages due to its larger HTF tube diameter and enhanced heat-transfer area, it has a smaller PCM volume, which limits its total thermal-energy storage capability. The primary objective of the present study is to maximize absorbed thermal energy rather than minimize melting time alone. In practical LHSS applications, a configuration that melts faster does not necessarily provide the highest energy storage capacity. The final optimized design proposed in this study (*OSTE*) achieves complete melting within the considered charging period (5 h) while simultaneously providing the highest energy absorption capability. Therefore, the selected configuration balances rapid thermal response and high storage capacity. Several factors limit the maximum achievable E_m, including the reduced temperature difference between the HTF and PCM during charging, the gradual weakening of the heat-transfer driving force as the PCM approaches complete melting, and the transition from conduction-dominated to convection-dominated heat-transfer mechanisms. Furthermore, excessive enhancement of melting rate through larger heat transfer surfaces may reduce the available PCM volume and consequently decrease the total stored energy. These physical limitations create a trade-off between rapid melting and high energy storage capacity, which the optimization framework of the present study considered.

Fig. 10(f) compares the average PCM temperature variations. Both optimized designs exhibit substantially higher temperatures than the core design throughout the melting. The *OSTE* shows slightly higher temperatures across the early development period and the subsequent mid-stage evolution due to its stronger heat concentration near the HTF channels. However, toward the final stages, the temperature difference between *OSTE* and *OLTE* decreases considerably, and both designs eventually approach nearly identical final temperatures. This behavior indicates that although the two optimized configurations follow different thermal pathways during charging, both achieve highly efficient thermal energy storage performance compared with the conventional core design.

8.7. Liquid fraction and temperature contours for the optimal designs

Fig. 11 represents the liquid fraction contours for the three investigated storage configurations, namely the core-design, *OSTE*, and *OLTE*, during the 5-h charging process. These contours provide a clear physical understanding of how the geometrical parameters influence melting behavior and thermal transport inside the LHSS. By observing the progression of the melting fronts, one can clearly distinguish the different

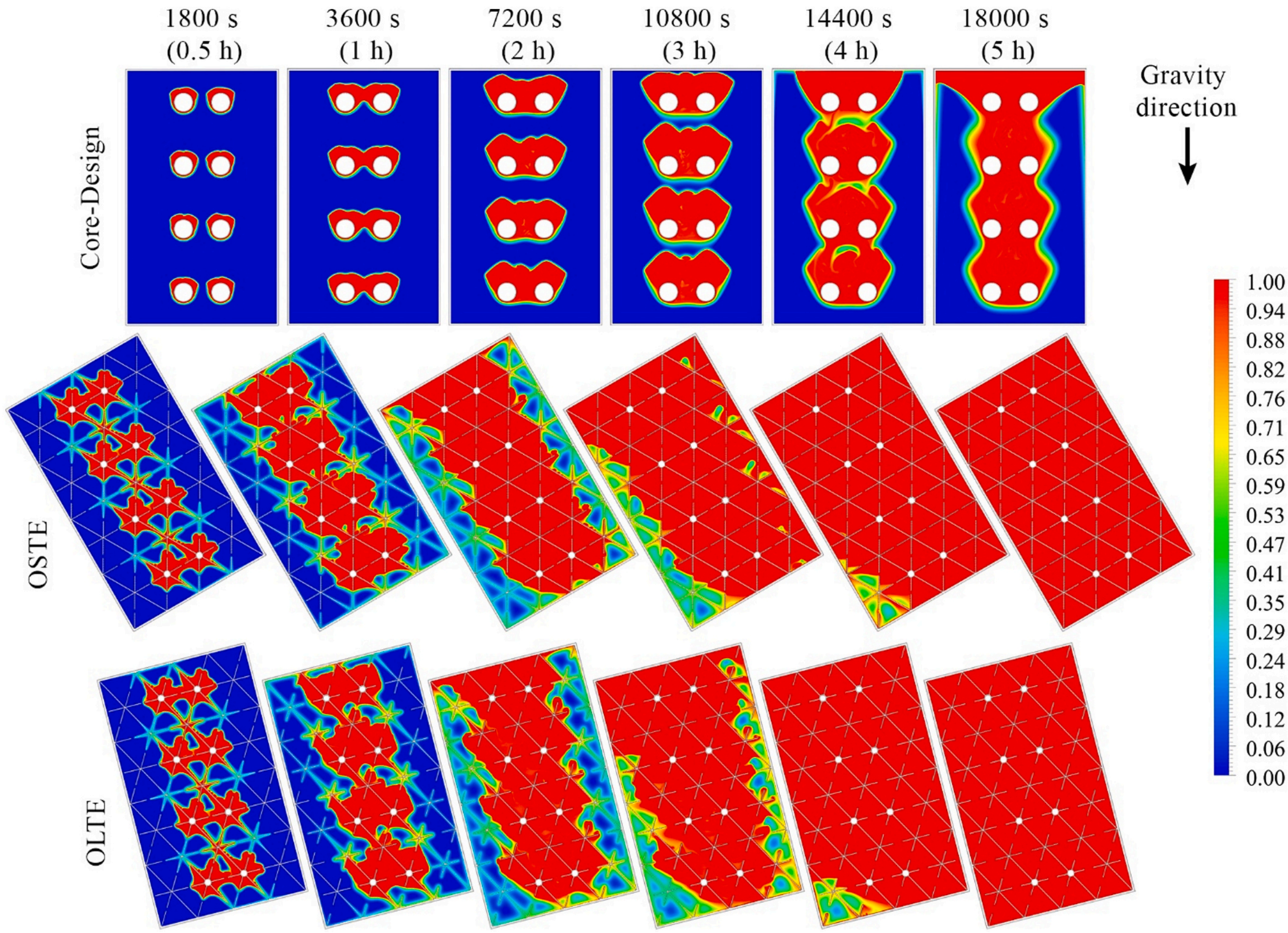

Fig. 11. Liquid fraction contours for the core-design, OSTE, and OLTE configurations.

thermal behaviors produced by variations in the geometrical parameters L, D, and α. The upper row corresponds to the core design, which contains only the HTF tubes without a perforated fin network. In this configuration, the melting process starts locally around the HTF tubes and gradually expands outward. Because no conductive fin structure distributes heat throughout the PCM domain, thermal energy transfer relies primarily on conduction during the initial stages and on natural convection after partial melting begins. Consequently, the melting process remains relatively slow and localized. Even after 7200 s (2 h), large regions of solid PCM are still visible around the storage body. The effect of gravity can also be clearly observed in the later stages. Due to buoyancy-driven flow, the molten PCM moves upward, causing faster melting near the upper regions while the lower sections remain partially solid longer. At 18000 s (5 h), although a large portion of the PCM has melted, considerable unmolten regions still exist near the side walls. This explains the previously observed weak thermal performance in the energy absorption plots for the core design.

The second row shows the *OSTE* configuration, optimized for short-term energy absorption. In this design, the storage body is inclined with a relatively larger α value, while the perforation length L is smaller. In addition, the HTF tube diameter D is moderate, maintaining a suitable balance between PCM volume and heat transfer area. The perforated network promotes efficient heat transfer from the HTF channels into the adjacent RT50, producing significantly larger molten regions even at early charging stages. At 1800 s (0.5 h), melting has already propagated deeply into the central sections of the storage body, unlike in the core design, where melting remains concentrated around the tubes. One of the most important observations in the *OSTE* contours is the concentration of molten PCM within the central regions. Because of the larger α value, the buoyancy-driven upward movement of molten PCM becomes partially restricted by the orientation of the fin network. The molten PCM tends to circulate and remain trapped near the middle sections before gradually passing through the perforations. As a result, thermal energy remains concentrated within the interior of the storage body rather than escaping rapidly into the upper sections. This phenomenon intensifies local heat transfer and accelerates short-term melting. Consequently, the *OSTE* configuration achieves extremely rapid melting progression and nearly complete melting before the other designs. By 10,800 s (3 h), most of the PCM has already melted, and after 14,400 s (4 h), the storage body becomes almost entirely liquid. This behavior explains why OSTE demonstrated superior short-term thermal performance in the previous energy-absorption analyses.

The third row illustrates the *OLTE* configuration, optimized for long-term energy absorption. Compared with *OSTE*, the *OLTE* design has a larger L, resulting in a larger PCM volume within the storage body. The larger PCM volume increases the total thermal energy storage capacity, although it slightly slows the melting rate during the initial stages. This behavior is clearly visible in the contours. At 1800 s and 3600 s, the melting front in *OLTE* develops more slowly than in *OSTE*, and larger solid regions remain inside the storage domain. However, the perforated fin network still provides more efficient heat distribution than the core design. The longer perforation length in *OLTE* creates wider pathways for molten PCM flow. Therefore, buoyancy-driven flow can rise more easily, allowing thermal energy to spread to the upper sections of the storage body more rapidly. Unlike *OSTE*, where energy tends to remain concentrated in the center, the *OLTE* configuration promotes more distributed melting across the entire domain. This leads to better utilization of the larger PCM volume during the later stages of charging. Although *OLTE* melts slightly more slowly initially, the increased PCM quantity enables greater total energy storage in the long term. By the final stages, the *OLTE* contours show highly uniform melting throughout the storage body, confirming the superior long-term thermal storage performance of this configuration.

The temperature contours in Fig. 12 provide a direct insight into how heat propagates inside the PCM and how geometrical parameters influence thermal performance. The color scale ranges from blue (298.15 K) to red (333.15 K), indicating low to high temperatures, respectively. Downward gravity plays an important role in buoyancy-driven convection. The core design represents the baseline configuration, in which the storage body contains only vertical HTF tubes without a perforated fin network. In the initial stages (1800–3600 s / 0.5–1 h), localized heating develops near the HTF tubes, forming confined high-temperature regions. The surrounding PCM remains largely cool, as heat transfer is dominated by conduction. The HTF tube diameter is moderate, allowing heat release but not enough to rapidly warm distant regions. At intermediate stages (7200–10,800 s / 2–3 h), buoyancy-driven natural convection becomes more pronounced, causing molten PCM to rise. Higher temperatures are observed near the top of the PCM domain, while lower regions, particularly at the sides and near the bottom, remain relatively cool. The absence of perforated fins limits lateral heat transfer, resulting in non-uniform temperature contours. At later stages (14400–18,000 s / 4–5 h), while a large portion of the PCM has melted and warmed significantly, the temperature distribution remains uneven. Cooler pockets persist near the side walls, and the right edge heats more slowly due to limited lateral heat conduction. This behavior explains the relatively weak thermal performance and lower energy-absorption efficiency observed in the core design compared to *OSTE* and *OLTE*.

In the *OSTE* configuration, temperature rises rapidly not only around the HTF tubes but also spreads efficiently through the perforated fins. Unlike the core design, the molten PCM is concentrated in the central regions due to the larger α angle, which partially directs the flow and partially restricts upward convection. The sides heat faster than in the core design, but peak temperatures remain centered. At intermediate stages, the central region reaches high temperatures quickly, and the surrounding PCM warms steadily. The combination of conduction through fins and buoyancy-driven convection along the perforation pathways accelerates heat transfer. By 10,800 s (3 h), most PCM samples show elevated temperatures, indicating rapid melting and energy absorption. At later stages, the temperature distribution approaches uniformity, though a slight concentration remains in the centre due to the design orientation. The *OSTE* configuration achieves nearly complete melting and high thermal energy density in a short time, highlighting its superior short-term performance.

In the *OLTE* design's initial stages, heating is slower than *OSTE* due to the larger volume of PCM (a small amount) and lower heat transfer surfaces. Temperatures near the HTF tubes rise first, while the rest of RT50, including the sides and bottom regions, remain relatively cooler.

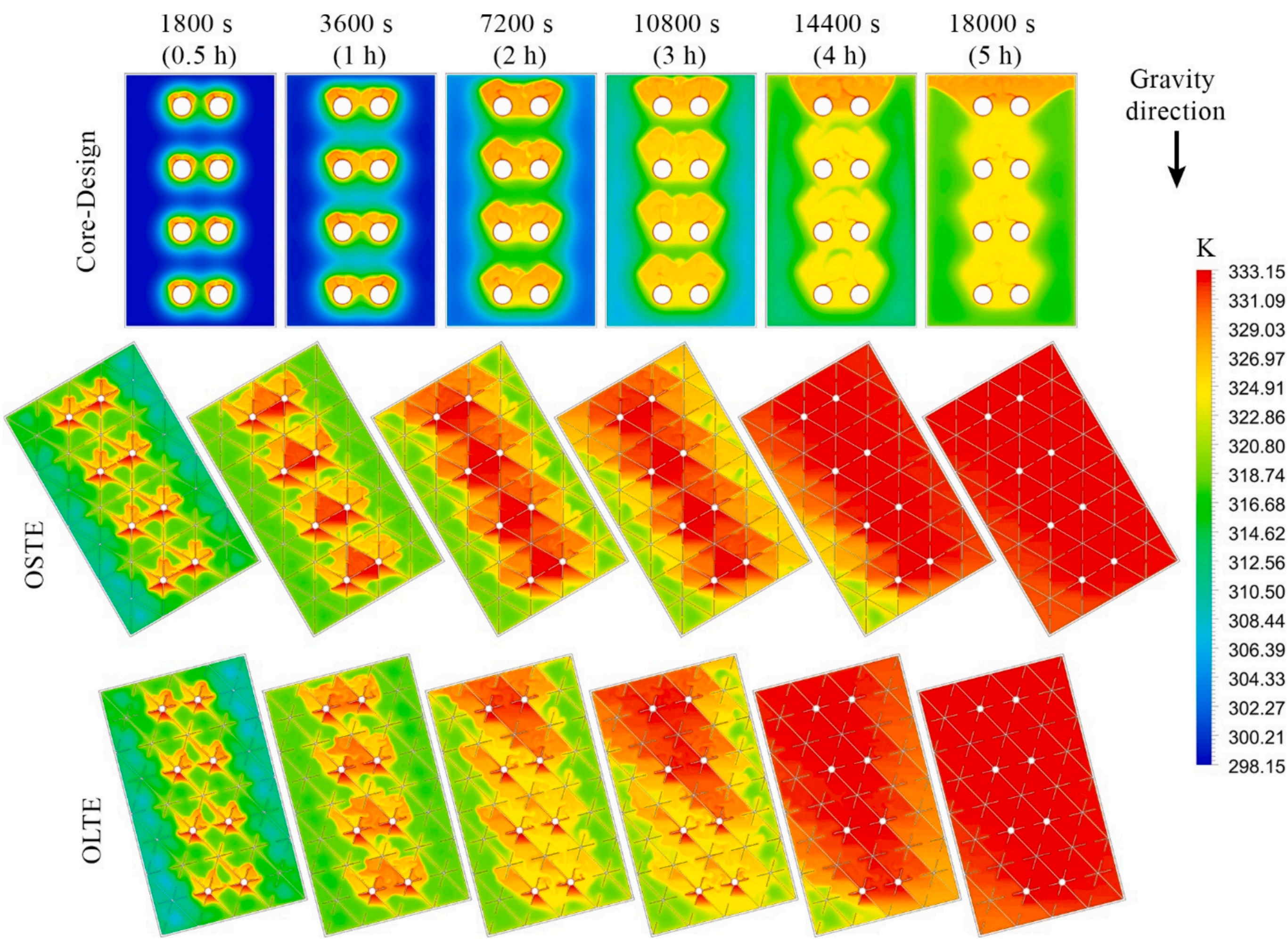

Fig. 12. Temperature contours in core-design, OSTE, and OLTE Configurations during 5-Hour Charging.

At intermediate stages, the perforated fins guide molten PCM along extended pathways, facilitating more uniform lateral and vertical heat distribution. The top-left side of the storage body warms steadily, and high-temperature zones spread across a larger fraction of the PCM. By the end of charging, the temperature field becomes highly uniform, including the storage body's edges and corners. The longer perforation length allows natural convection to distribute heat more efficiently, while the greater PCM volume enhances long-term energy storage. The *OLTE* design therefore provides the best combination of uniform heating and high total energy storage, although it initially melts slightly more slowly than *OSTE*. Although the *OLTE* configuration absorbs slightly more energy under long-term operating conditions, the difference between *OLTE* and *OSTE* is relatively small. The additional energy absorbed by *OLTE* is only about 53 kJ, which is insignificant compared to the device's overall thermal storage capacity. In contrast, the *OSTE* configuration demonstrates a substantially faster energy absorption rate throughout most stages of the charging process. Therefore, the thermal advantage of *OSTE* during short-term and intermediate melting stages is considerably more meaningful from a practical engineering perspective than the very small long-term improvement achieved by *OLTE*. Considering these observations, along with the results from the multi-objective optimization and TOPSIS analyses, the *OSTE* configuration is the most suitable and balanced design among the investigated configurations.

9. Conclusions

This study introduced a novel perforated fin-assisted latent heat storage system and comprehensively investigated its thermal performance through numerical analysis, machine learning prediction, and optimization approaches. The proposed interconnected perforated fin network significantly enhanced heat transfer within the PCM domain by simultaneously improving conductive pathways and promoting natural convection through strategically distributed openings.

- Compared with the core design without perforated fins, the proposed configurations demonstrated remarkable improvements in energy absorption capability. Specifically, the best-performing design during the intermediate charging stage absorbed 7763 kJ of thermal energy after 9000 s, whereas the reference configuration stored only 3077 kJ, corresponding to an enhancement of approximately 153.2%. Furthermore, after 18,000 s of charging, the optimized fin-assisted configurations achieved nearly 9957 kJ of absorbed energy, while the core design absorbed only 5395 kJ, representing an improvement of approximately 84.6%.
- The results showed that the optimal geometry depends strongly on the charging stage and the dominant heat transfer mechanism. The configuration with shorter perforation length and smaller HTF tube diameter performed better during the early and intermediate stages because of enhanced conductive heat transfer and improved thermal interaction between the PCM and fin network. However, during the later stages of melting, configurations with stronger natural convection pathways achieved higher overall energy absorption due to more effective thermal redistribution within the molten PCM region. These findings highlight that a single geometric configuration may not provide the optimum performance throughout the entire charging process, and the selection of design parameters should consider the targeted operating duration.
- Moreover, the developed MLP model successfully captured the nonlinear relationship between geometrical parameters and thermal performance indicators, providing an efficient prediction tool for rapid performance evaluation. Coupling the MLP model with GA optimization and TOPSIS decision-making enabled identification and ranking of favorable configurations without requiring extensive additional numerical simulations. Therefore, the proposed integration of advanced fin architecture with data-driven optimization provides a promising framework for designing efficient PCM-based latent heat storage systems for renewable energy applications.

Although the proposed system demonstrated significant thermal enhancement, further investigations are required to improve its practical applicability. Future studies can focus on evaluating alternative HTF tube arrangements and configurations to optimize heat distribution within the storage domain further. In addition, the internal topology of the fin network, including fin arrangement, spacing, thickness, and perforation characteristics, can be modified to achieve improved thermal performance while maintaining a high PCM storage volume. The use of industrial PCMs with higher thermal conductivity, as well as the incorporation of nanoparticles or metal foams into PCM structures, can also be explored to further enhance heat-transfer characteristics. Furthermore, investigation of the solidification process and the coupled charging/discharging performance under cyclic operating conditions would provide deeper insights into the long-term reliability and practical implementation of the proposed latent heat storage system.

CRediT authorship contribution statement

Motrih Al-Mutiry: Resources, Project administration, Investigation. **Hyder H. Abed Balla:** Investigation, Formal analysis. **Mohamed Arbi Khlifi:** Formal analysis, Data curation. **Banaz Shahab Haji:** Writing – review & editing, Investigation. **Mohammad Abdulhadi O. Althobaiti:** Writing – review & editing, Writing – original draft. **Ashrf althbiti:** Validation, Data curation. **Norah Alsairy:** Validation, Formal analysis. **Hanaa Abu-Zinadah:** Supervision, Investigation. **Duc Chuan Nguyen:** Investigation, Conceptualization. **Ibrahim Mahariq:** Writing – original draft, Supervision, Methodology.

Declaration of competing interest

The authors declare that they have no known competing financial interests or personal relationships that could have appeared to influence the work reported in this paper.

Acknowledgement

This research was funded by Princess Nourah bint Abdulrahman University Researchers Supporting Project number (PNURSP2026R241), Princess Nourah bint Abdulrahman University, Riyadh, Saudi Arabia.

Data availability

The authors do not have permission to share data.

References

[1] A.I. Almulhim, I.R. Abubakar, The role of renewable energy in achieving the sustainable development goals: a systematic review and conceptual framework, Renew. Sust. Energ. Rev. 230 (2026) 116679, https://doi.org/10.1016/j.rser.2025.116679.
[2] Q. Wang, S. Zhang, R. Li, Artificial intelligence in the renewable energy transition: the critical role of financial development, Renew. Sust. Energ. Rev. 226 (2026) 116280, https://doi.org/10.1016/j.rser.2025.116280.
[3] X. Wang, L. Ye, C. Liu, X. Liang, T. Zheng, C. Yao, Investigation of cooling performance and robustness of laid-back fan-shaped holes affected by internal roughness, Int. J. Heat Mass Transf. 253 (2025) 127605, https://doi.org/10.1016/j.ijheatmasstransfer.2025.127605.
[4] F. Esmaeilion, S. Hoseinzadeh, S. Shafiei, E. Pilali, A. Taklifi, M. Soltani, et al., Review of renewable energy-based products application for battery thermal management, Renew. Sust. Energ. Rev. 226 (2026) 116247, https://doi.org/10.1016/j.rser.2025.116247.
[5] H. Li, H. Zhang, X. Wu, X. Niu, W. Hong, H. Li, Enhanced vapor condensation in bidirectional solar stills using copper foam with multiple nucleation sites, Sci. China Technol. Sci. 69 (2026) 1920106, https://doi.org/10.1007/s11431-025-3248-5.
[6] D. Bredemeier, S. Khalili, D. Keiner, C. Breyer, Prospects for solar photovoltaics in highly renewable energy transition scenarios towards a dominant future energy

source, Renew. Sust. Energ. Rev. 235 (2026) 116934, https://doi.org/10.1016/j.rser.2026.116934.

[7] L. Vallese, H. Javadi, B. Badenes, J.F. Urchueguia, G. Lombardo, D. Menegazzo, et al., A comprehensive review of thermal energy storage technologies and their applications: creation of a database, Renew. Sust. Energ. Rev. 225 (2026) 116133, https://doi.org/10.1016/j.rser.2025.116133.

[8] Q. Lin, R. Yan, M. Huang, Y. Chen, L. Zhang, T. Yin, et al., Multi-source responsive and leakage-proof phase change composites based on cellulose nanofiber/sodium alginate crosslinked aerogel for thermal energy storage and management, Int. J. Biol. Macromol. 349 (2026) 150980, https://doi.org/10.1016/j.ijbiomac.2026.150980.

[9] X. Wang, Y. Zhou, C. Yang, Y. Zhou, F. Liu, Thermochromic phase change materials: optical – thermal coupling, fabrication, and applications — a review, Sol. Energy Mater. Sol. Cells 306 (2026) 114531, https://doi.org/10.1016/j.solmat.2026.114531.

[10] S. Nekahi, F.S. Moghanlou, M. Vajdi, K. Vaferi, S. Nekahi, T. Gholizadeh, Development and performance evaluation of a honeycomb-structured shell-and-tube thermal storage system integrating a series of openings on the hexagonal cells for enhanced energy absorption/release, Int. Commun. Heat Mass Transfer 173 (2026) 110897, https://doi.org/10.1016/j.icheatmasstransfer.2026.110897.

[11] N.P. Tran, T.D. Ngo, Concrete-based thermal energy storage (CTES) for concentrated solar power plants and built environment, Renew. Sust. Energ. Rev. 230 (2026) 116692, https://doi.org/10.1016/j.rser.2025.116692.

[12] T.K. Şener, G. Çakmak, A specialized multi-model adaptive network-based fuzzy inference system approach for optimizing latent heat storage systems from sparse experimental data, J. Energy Storage 147 (2026) 120311, https://doi.org/10.1016/j.est.2025.120311.

[13] L. Naik, V. Gumtapure, Numerical and experimental investigation with response surface methodology optimization of melting behavior of nanoparticle-dispersed PCM in horizontal shell and spiral coil latent heat thermal energy storage system, Results Eng. 29 (2026) 108849, https://doi.org/10.1016/j.rineng.2025.108849.

[14] J. Li, G. Chen, Y. Hu, Z. Zhang, Z. Zhao, H. Jiang, et al., Optimizing turbulent heat transfer modeling of low-Prandtl-number negatively buoyant jets: data assimilation and solution strategy assessment, Int. Commun. Heat Mass Transfer 177 (2026) 111522, https://doi.org/10.1016/j.icheatmasstransfer.2026.111522.

[15] K. Vaferi, A. Farajollahi, T. Gholizadeh, M. Rostami, Enhancing charging and discharging performance in a novel latent heat storage via design optimization and artificial neural network modeling, J. Energy Storage 114 (2025) 115757, https://doi.org/10.1016/j.est.2025.115757.

[16] H.M. Hanif, M. Tayyeb, M. Awais, R.M. Hafez, Z. Jastaneyah, H.A.L. Garalleh, et al., Analysis of solar heating system integrated with latent heat storage, Comput. Biol. Med. 210 (2026) 111698, https://doi.org/10.1016/j.compbiomed.2026.111698.

[17] S.A. Yazdanparast, M. Setareh, H. Basirat Tabrizi, Numerical investigation of melting characteristics of fin-assisted single and dual PCM latent heat storage system under time-dependent solar heat flux, Discov. Mech. Eng. 5 (2026) 14, https://doi.org/10.1007/s44245-026-00185-z.

[18] Q. Wang, Z. Xu, W. Jia, X. Song, G. Li, M. Zhou, et al., Active wellbore cooling during deep drilling circulation via microencapsulated phase change materials: energy redistribution mechanism and inverse design, Energy 360 (2026) 141647, https://doi.org/10.1016/j.energy.2026.141647.

[19] X. Liu, H.I. Mohammed, A.Z. Ashkezari, A. Shahsavar, A.K. Hussein, S. Rostami, An experimental investigation on the rheological behavior of nanofluids made by suspending multi-walled carbon nanotubes in liquid paraffin, J. Mol. Liq. 300 (2020) 112269, https://doi.org/10.1016/j.molliq.2019.112269.

[20] M.A. Said, H. Togun, A.M. Abed, N. Biswas, H.I. Mohammed, H.S. Sultan, et al., Evaluation of wavy wall configurations for accelerated heat recovery in triplex-tube energy storage units for building heating applications, J. Build. Eng. 94 (2024) 109762, https://doi.org/10.1016/j.jobe.2024.109762.

[21] A. Bahlekeh, H.I. Mohammed, W.K. Al-Azzawi, A. Dulaimi, H.S. Majdi, P. Talebizadehsardari, et al., CFD analysis on optimizing the annular fin parameters toward an improved storage response in a triple-tube containment system, Energy Sci. Eng. 10 (2022) 4814–4839, https://doi.org/10.1002/ese3.1310.

[22] A. Godin, F. Salmon, A. Perro, D. Lacanette, J.-L. Faure, M. Duquesne, Real data based and highly-resolved simulation of the anisotropic heat transfer within packed-bed PCM storage systems for urban heating networks, Int. J. Therm. Sci. 227 (2026) 110895, https://doi.org/10.1016/j.ijthermalsci.2026.110895.

[23] F.H. Ali, Q.R. Al-Amir, H.K. Hamzah, L. Kolsi, Numerical investigation of nano-PCM latent-sensible thermal energy storage enclosures, Int. Commun. Heat Mass Transfer 172 (2026) 110548, https://doi.org/10.1016/j.icheatmasstransfer.2026.110548.

[24] K. Vaferi, S. Nekahi, S. Nekahi, H. Ghaebi, Charging/discharging performance examination in a finned-tube heat storage tank: based on artificial neural network, Pareto optimization, and numerical simulation, Case Stud. Therm. Eng. (2025) 106388, https://doi.org/10.1016/j.csite.2025.106388.

[25] F. Alimi, N.H. Alrasheedi, M.H. Heidarshenas, M. Bouzidi, M. Mohamed, K. Hajlaoui, et al., Triangular-shell finned latent heat storage: orientation and fin-design effects, Case Stud. Therm. Eng. 78 (2026) 107624, https://doi.org/10.1016/j.csite.2025.107624.

[26] A.T. Hoang, V.V. Pham, X.P. Nguyen, Integrating renewable sources into energy system for smart city as a sagacious strategy towards clean and sustainable process, J. Clean. Prod. 305 (2021) 127161, https://doi.org/10.1016/j.jclepro.2021.127161.

[27] Y. Lu, H. Zhang, Z. Wang, S. Wu, A novel latent heat thermal energy storage unit with fractal arrow fins for efficient thermal utilization, J. Energy Storage 155 (2026) 121539, https://doi.org/10.1016/j.est.2026.121539.

[28] R.Z. Homod, H.I. Mohammed, A.M. Sadeq, B.N. Alhasnawi, A.W. Al-Fatlawi, A. Al-Manea, et al., Massive energy reduction and storage capacity relative to PCM physical size by integrating deep RL clustering and multi-stage strategies into smart buildings to grid reliability, J. Energy Storage 109 (2025) 115058, https://doi.org/10.1016/j.est.2024.115058.

[29] Y. Wu, H.I. Mohammed, S. Chen, M. Luo, Y. Yu, Z. Zhou, Numerical investigation of the impact of toothed fins on the heat transfer performance of a shell-and-tube exchanger during phase change material melting process, Int. J. Heat Mass Transf. 217 (2023) 124637, https://doi.org/10.1016/j.ijheatmasstransfer.2023.124637.

[30] Saini P. Niketan, A. Dhar, S. Powar, Parametric optimization and charging performance enhancement of X-fin employed shell and tube solid-solid PCM based latent heat thermal energy storage system, J. Energy Storage 152 (2026) 120356, https://doi.org/10.1016/j.est.2026.120356.

[31] S. Tang, P. Liu, Y. Song, H. Xi, X. Wu, X. Yang, et al., Solidification performance enhancement of a latent heat thermal energy storage system: a novel discontinuous fin configuration for vertical shell-and-tube design, Renew. Energy 261 (2026) 125275, https://doi.org/10.1016/j.renene.2026.125275.

[32] J.-B. Mao, A. Basem, H.H. Abed Balla, O.J. Alkhatib, Y. Elmasry, Y. Li, et al., Triangular-rib structural mastery for enhanced latent heat storage system: artificial neural network optimization of geometry, orientation, and cost-effectiveness, J. Energy Storage 152 (2026) 120463, https://doi.org/10.1016/j.est.2026.120463.

[33] M.A. Alnakeeb, W.M. Galal, M.E. Youssef, M.A. Abdel Salam, M.M. Sorour, Melting performance assessment of a latent thermal energy storage unit with multiple oriented elliptic tubes in various arrangements, J. Energy Storage 140 (2025) 119111, https://doi.org/10.1016/j.est.2025.119111.

[34] W. Deng, J. Li, S. Samad, A.M. Abed, A. Almadhor, S. Alhumaid, et al., Optimization and prediction of heat absorption in a modular multi-section latent heat storage system with dome-shaped components using a multilayer perceptron model, TOPSIS analysis, and Pareto fronts, J. Energy Storage 131 (2025) 117542, https://doi.org/10.1016/j.est.2025.117542.

[35] S. Zhang, W. Hu, G. Liu, L. Pu, Design method and parameters optimization of finned-tube latent thermal energy storage for heat pump applications, Int. J. Refrig. 186 (2026) 106882, https://doi.org/10.1016/j.ijrefrig.2026.02.025.

[36] M. Vajdi, K. Vaferi, Thermal–hydraulic performance analysis and optimization of a recuperator via geometric modification using numerical simulation and artificial neural networks, Results Eng. 30 (2026) 111058, https://doi.org/10.1016/j.rineng.2026.111058.

[37] S.F. Ahmed, N. Rafa, T. Mehnaz, B. Ahmed, N. Islam, M. Mofijur, et al., Integration of phase change materials in improving the performance of heating, cooling, and clean energy storage systems: an overview, J. Clean. Prod. 364 (2022) 132639, https://doi.org/10.1016/j.jclepro.2022.132639.

[38] N. Hanchi, R. Elbahjaoui, Enhancement of thermal energy storage performance in rectangular latent heat systems through coupling of cascaded phase change materials and fins, Appl. Therm. Eng. 300 (2026) 131422, https://doi.org/10.1016/j.applthermaleng.2026.131422.

[39] A.M. Ali, A. Bagdanavicius, A. Rona, S. Shahzad, Enhanced solidification in latent heat storage systems using fins and twisted tapes, Therm. Sci. Eng. Prog. 74 (2026) 104718, https://doi.org/10.1016/j.tsep.2026.104718.

[40] X. Gang, Y. Fu, N. Gascoin, C. Wang, H. Zhou, G. Xu, A physically motivated feature engineering and proxy validation strategy for XGBoost-based reconstruction of thermal conductivity in supercritical hydrocarbon fluids, Int. Commun. Heat Mass Transfer 178 (2026) 111846, https://doi.org/10.1016/j.icheatmasstransfer.2026.111846.

[41] Y. Hong, Y. Shi, Q. Li, T. Xie, C. Xiao, J. Du, Heat transfer and energy storage performances enhanced by bionic fin structures in a rectangular latent heat storage unit: a comparative study, Int. J. Heat Fluid Flow 119 (2026) 110311, https://doi.org/10.1016/j.ijheatfluidflow.2026.110311.

[42] M. Mahboobtosi, F.N. Chari, H. Ehsani, D.D. Ganji, Artificial intelligence-GFEM approach for predicting VIFs impact on HNEPCM solidification in hexagonal latent heat thermal energy storage systems with solar radiation, Appl. Therm. Eng. 298 (2026) 131110, https://doi.org/10.1016/j.applthermaleng.2026.131110.

[43] T. Zhao, J. Wei, S. Du, H. Shan, R. Wang, A physics-informed neural network framework for state estimation of latent heat thermal energy storage: temperature reconstruction and state-of-charge prediction, Energy Convers. Manag. 351 (2026) 121051, https://doi.org/10.1016/j.enconman.2026.121051.

[44] S. Khalid, M.A. Khan, H. Waqas, D. Liu, Artificial neural network for melting enhancement of nano-enhanced PCM in triplex tubes, Int. Commun. Heat Mass Transfer 173 (2026) 110743, https://doi.org/10.1016/j.icheatmasstransfer.2026.110743.

[45] S. Yin, X. Wang, W. Li, B. Xu, Numerical investigation on effects of interactions between particles on coating formation in cold spraying, J. Therm. Spray Technol. 18 (2009) 686–693, https://doi.org/10.1007/s11666-009-9390-6.

[46] R. Smith, H. Inomata, C. Peters, Heat Transfer and Finite-Difference Methods, 2013, pp. 557–615, https://doi.org/10.1016/B978-0-444-52215-3.00008-8.

[47] S. Zhang, Y. Hong, G. Liu, L. Pu, Topology-optimized fin design for enhanced latent thermal energy storage in laser thermal management, Int. J. Heat Mass Transf. 261 (2026) 128529, https://doi.org/10.1016/j.ijheatmasstransfer.2026.128529.

[48] V.N. Nguyen, W. Tarełko, P. Sharma, A.S. El-Shafay, W.-H. Chen, P.Q.P. Nguyen, et al., Potential of explainable artificial intelligence in advancing renewable energy: challenges and prospects, Energy Fuel 38 (2024) 1692–1712, https://doi.org/10.1021/acs.energyfuels.3c04343.

[49] A.A. Khalaf, H. Togun, Heat transfer enhancement in thermal energy storage using novel fin designs: a numerical study, J. Energy Storage 163 (2026) 122054, https://doi.org/10.1016/j.est.2026.122054.

[50] B. Agegnehu, A. Ribezzo, A. Bottega, M. Morciano, M. Fasano, E. Chiavazzo, Rotating fins in phase change materials for cyclable high-power density latent thermal energy storage, J. Energy Storage 160 (2026) 121877, https://doi.org/10.1016/j.est.2026.121877.

[51] A. Jahanbin, U. Berardi, Rotationally staggered elliptical-fin architecture for thermal enhancement of horizontal latent thermal energy storage systems, Therm. Sci. Eng. Prog. 71 (2026) 104488, https://doi.org/10.1016/j.tsep.2026.104488.

[52] N.A.A. Qasem, A. Belazreg, Y. Khetib, O. Younis, A. Abderrahmane, Enhancing heat transfer in latent thermal storage: synergistic effects of multi-tube flow, arc fins, and Cu nanoparticles, J. Energy Storage 161 (2026) 121870, https://doi.org/10.1016/j.est.2026.121870.

[53] A. Yawar, J. Mohammadpour, F. Salehi, A novel integrated computational framework for optimizing fin-enhanced triplex-tube latent thermal energy storage, J. Energy Storage 163 (2026) 122009, https://doi.org/10.1016/j.est.2026.122009.

[54] R. Zhang, W. He, H. Gan, C. Liu, J. Zhao, Novel heat pipe/PCM/fins coupled system for efficient thermal energy storage and stable heating: an experimental investigation, Appl. Therm. Eng. 289 (2026) 129809, https://doi.org/10.1016/j.applthermaleng.2026.129809.

[55] H. Kaya, E. Alp, S. Sabet, B. Buonomo, L. Fedele, S. Rossi, et al., Experimental investigation of thermal performance of NanoEncapsulated-PCM emulsions in parallel plate thermal energy storage system, Int. Commun. Heat Mass Transfer 170 (2026) 110009, https://doi.org/10.1016/j.icheatmasstransfer.2025.110009.

[56] A. Verma, R. Kukreja, T. Srinivas, D. Buddhi, Experimental investigation of triplex-tube latent heat thermal energy storage system incorporating a helical coil for thermal performance enhancement, Energy Technol. 14 (2026), https://doi.org/10.1002/ente.202501472.

[57] C.-Y. Zhao, X.-S. Zhao, S.-Q. Wang, C.-Y. Jia, D. Qi, J.-M. Jiang, Mechanism-driven design of gradient porous metal foam/PCM composites in a triplex-tube helical-coiled thermal energy storage unit, Renew. Energy 266 (2026) 125729, https://doi.org/10.1016/j.renene.2026.125729.

[58] M. Mahboobtosi, K. Hosseinzadeh, S. Faghiri, M. Soleymanzadeh, D.D. Ganji, Optimized branched fin design and combined nanoparticles for faster solidification of phase change materials in a triple-tube thermal energy storage system, J. Energy Storage 154 (2026) 121229, https://doi.org/10.1016/j.est.2026.121229.

[59] N. Kousha, M. Rahimi, R. Pakrouh, R. Bahrampoury, Experimental investigation of phase change in a multitube heat exchanger, J. Energy Storage 23 (2019) 292–304, https://doi.org/10.1016/j.est.2019.03.024.

[60] Y. Wang, Z. Xu, Y. Fu, S. Liu, Y. Shen, W. Ji, et al., A novel optimized control strategy based on BP neural network for dynamic heating of sorption energy storage system, J. Energy Storage 141 (2026) 119180, https://doi.org/10.1016/j.est.2025.119180.

[61] R.K. Singh, R. Shankar, V. Verma, Hybrid energy storage systems with innovative artificial neural network-based controller for strengthening power system resilience, J. Energy Storage 153 (2026) 120824, https://doi.org/10.1016/j.est.2026.120824.

[62] A. Mohamed, E.M. Wazeer, S.M. El Masry, A.M.A. Ghany, M.A. Mosa, Artificial neural network control of virtual inertia-based energy storage for frequency regulation in multi-microgrid considering communication delay, J. Energy Storage 152 (2026) 120535, https://doi.org/10.1016/j.est.2026.120535.

[63] A. Tang, Z. Tong, C. Hu, C. Ding, Y. Shang, L. Ma, et al., Research on grid-forming control strategy of modular multilevel converter energy storage systems based on passivity-based control-sliding mode control-PID neural network, J. Energy Storage 147 (2026) 119986, https://doi.org/10.1016/j.est.2025.119986.

[64] A. Boubakir, M.A. Ahmed, S. Labiod, T. Souanef, Design of a robust adaptive neural network MPPT controller for a photovoltaic energy storage system, J. Control Autom. Electr. Syst. 37 (2026) 362–378, https://doi.org/10.1007/s40313-025-01234-w.

[65] A.V. Vykhodtsev, F. ShakeriHosseinabad, D. Jang, Q. Wang, W. Rosehart, H. Zareipour, Artificial intelligence-assisted physics-based model of lithium-ion battery for power systems operation research, J. Energy Storage 151 (2026) 120563, https://doi.org/10.1016/j.est.2026.120563.

[66] H. Benfatma, H. Khouidmi, B. Bessedik, Neural network and ACO algorithm-tuned PI controller for MPPT in a hybrid battery-supercapacitor energy storage system within DC micro-grid photovoltaic installations, J. Energy Storage 120 (2025) 116499, https://doi.org/10.1016/j.est.2025.116499.